PIEZOELECTRIC PRESSURE SENSORS BASED ON FLEXIBLE PZT THICK-FILM COMPOSITE DEVICE

by

Rongjie Liang

Bachelor of Mechanical Engineering, Wuhan University of Technology, 2012

Submitted to the Graduate Faculty of

Swanson School of Engineering in partial fulfillment

of the requirements for the degree of

Master of Science

University of Pittsburgh

2014

UNIVERSITY OF PITTSBURGH

SWANSON SCHOOL OF ENGINEERING

This thesis was presented

by

Rongjie Liang

It was defended on

November 24, 2014

and approved by

William S. Slaughter, Ph.D., Associate Professor, Department of Mechanical Engineering and Material Science

Patrick Smolinski, Ph.D., Associate Professor, Department of Mechanical Engineering and Material Science

Thesis Advisor: Qing-Ming Wang, Ph. D, Professor, Department of Mechanical Engineering and Materials Science

PIEZOELECTRIC PRESSURE SENSORS BASED ON FLEXIBLE PZT THICK-FILM COMPOSITE DEVICE

Rongjie Liang, M.S.

University of Pittsburgh, 2014

In this thesis, piezoelectric diaphragm pressure sensors have been proposed and developed. The piezoelectric Lead Zirconate Titanate (PZT) thick film was used in this sensor as sensing element due to its good piezoelectric property and mechanical flexibility. This kind of PZT thick film was fabricated recently using a tape-casting processing. By this process the PZT film thickness can be controlled in the range from tens to hundreds microns, making the novel flexible PZT diaphragm sensor realizable. Two structures of pressure sensor were designed and fabricated, and the relationship between generated voltage signals to applied pressures of the electromechanical model has been analyzed theoretically. For sandwiched structure sensor, the properties of the sensor to measure low frequency fluctuating pressures have been investigated experimentally. A test setup was designed and applied to generate pulsing fluid pressure waves and calibrate the sensitivities of sensor samples. The proposed pressure sensor exhibited highly sensitive response to low frequency dynamic pressure loading. The effectiveness of this sensor in human arterial pulse monitoring was studied and reported. For pressure sensor with unimorph structure, a blast wave pressure test was conducted using shock tube setup to study its sensing ability to intensive, transient pressure loading. Different sized sensors were tested and showed almost linear relationship to blast pressure in the given range.

TABLE OF CONTENTS

LIST OF TABLES

LIST OF FIGURES

PREFACE

I would like to extend my sincerest appreciation to my thesis advisor, Dr. Qing-Ming Wang, for all of his encouragement, support and guidance in this work and over the past two years of my M.S. study. I am very thankful to Dr. William S. Slaughter and Dr. Patrick Smolinski for their kindly willingness to serve as my committee members, and Dr. Jeffery Vipperman for his generous support in experiment equipment.

Meanwhile, I would like to thank my colleagues, Hongfei Zu, Huiyan Wu, Qiuyan Li, Zheng Min, Wenbin Luo for their help in my research.

I also thank the senior design group members, Abigail Sedlmeyer, Roland Beard, Ryan Waldron, Xuekun Xie, Shiyi Li, and machine shop staff, Andy Holmes, Thorin Tobiassen, for their help in the setup design and fabrication.

Finally, I would like to express my deepest gratitude to my families and my girlfriend, who are always supporting me and loving me in my life.

1.0 INTRODUCTION

Pressure sensing technology has been widely applied in human's daily life: monitoring of pressure magnitude and fluctuation is very important and necessary in many systems such as water pipeline, oil tank, engine combustion chamber and tire of vehicle, blood and respiration system of human body, etc.[1-5] Over past decades, many kinds of pressure sensors were developed. Generally there are three types of pressure sensor: capacitive, piezoresistive and piezoelectric sensors. Capacitive sensor uses a diaphragm-cavity structure as a capacitor to detect the air gap change caused by applied pressure, thus the difference of capacity indicates the pressure magnitude. This type of pressure sensor has a relative simple structure and high sensitivity, but can only detect low pressure and typically require high voltage operation. Piezoresistive sensor, which is the most common type for general purpose pressure measurement, detects strain due to pressure loading that results in resistance changes. Large power requirement, significant temperature dependence offset and slow response to dynamic pressure are drawbacks of piezoresistive sensor. Piezoelectric sensor generates detectable charge signal by itself in responding to applied pressure, displaying some advantages over other types of pressure sensors, such as self-powering, fast response of highly dynamic load, and relatively simple readout circuit. Generally, piezoelectric sensor has a diaphragm structure, which is the most effective design for pressure sensing. And it is ideal for measuring fluctuating input pressure signal.

Among various piezoelectric materials, lead zirconium titanate (PZT) has relative high piezoelectric charge constant and electromechanical coupling effect, which is favorable for pressure sensing. However, the brittleness nature of PZT makes it is much harder to be fabricated as a diaphragm structure as compared with other more flexible piezoelectric materials such as PVDF polymer, and ZnO thin film. Recent development in the fabrication of thick-film PZT ceramic with thickness about several tens of micrometers using tape-casting processing [20] makes it possible for the design and fabrication of flexible piezoelectric pressure sensors. In this thesis, PZT thick-film composite sensor was investigated and presented. Two structures of sensor were studied. Sandwiched structure sensor is used to detect pressure fluctuated under low frequency such as human blood pressure and pulsation, and unimorph structure senor to test blast wave pressure. Specific testing setup were designed and fabricated to calibrate these two kinds of sensors, respectively. In the following chapters, the background about piezoelectric sensor, PZT thick film material and device fabrications, experiment process and results will be presented.

2.0 BACKGROUND

2.1 FUNDAMENTAL BACKGROUND OF PIEZOELECTRICITY AND PRESSURE MEASUREMENT PRINCIPLE

The piezoelectricity was first discovered and demonstrated in 1880 by the brothers Pierre Curie and Jacques Curie. While investigating some naturally occurring materials such as tourmaline and quartz, Pierre and Jacques Curie realized that these materials have the ability to transform energy of mechanical input into an electrical output [6]. Then, with the development of science and technology, a number of man-made piezoelectric materials were introduced and fabricated such as BaTiO3 (Barium Titanate), Zinc Oxide (ZnO), lead zirconate Titanate (PZT) and poly vinylidene fluoride (PVDF). More specifically, when a pressure [piezo is the Greek word for pressure] is applied to a piezoelectric material, it causes a mechanical deformation and a displacement of charges. Piezoelectric materials undergo a dipole deformation and electric charges accumulation in response to applied mechanical stress. An electric field will generate and thus voltage can be detected on the upper and lower surface of the piezoelectric materials. When stress is removed, the voltage will disappear. This phenomenon is called direct piezoelectric effect. Conversely, the internal generation of mechanical strain of the piezoelectric material resulting from an applied electrical field is called reverse piezoelectric effect.

As we know, external loading on a unit cell of crystalline material without center symmetry will change its internal dipole moment. For example, Figure 2-1 (a) shows the structure of a unit cell of a Quartz crystal. When there is no applied stress on the crystal, the three electric dipole moments are distributed at 120° angle between each other and the central of positive and negative electrons coincide, generating no any charge on the surface of crystal. In Figure2-1(b) and (c), as the stress along x-direction applied, the vector sum of three electric dipole moments will be nonzero along the x-direction, resulting in the separation of positive and negative electrons' centers. Thus charges generate on the surface of the unit cell along the x-direction. Similarly, stress along y or z-direction also causes charges along x-direction. Thus x-direction is called the polarization direction for this crystal. Net polarization can be generated by externally applied stress for quartz crystal.

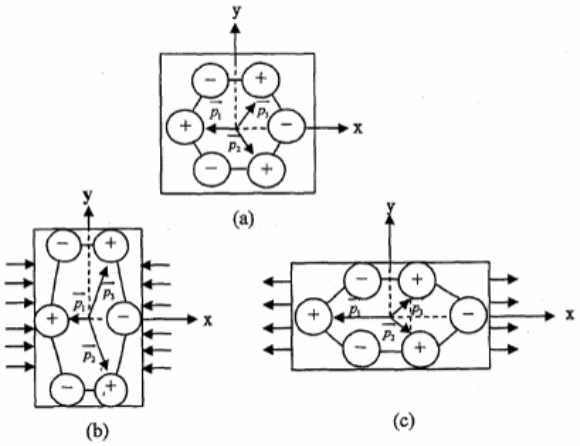

Figure 2-1. Schematic of piezoelectric effect [7]

For polycrystalline materials such as barium titanate (BaTiO3), lead titanate (PbTiO3), and lead zirconate titanate (PZT) ceramics, polarization directions of all unit cells are randomly distributed throughout a crystal material, as shown in Figure2-2 (a). Hence the diploes generated within unit cells will cancel each other and net polarization of the material will be almost zero no

matter how external stress applies. To produce a net polarization in these ceramic materials, a poling process can be applied: under a certain temperature (must lower than the paraelectric-ferroelectric phase transition temperature or Curie temperature), applying a large dc electric field on the material along a certain direction (Figure 2.2(b)) and then removed. A remnant polarization will be generated in these ferroelectric materials, as shown in Figure 2.2(c). This process is often called poling.

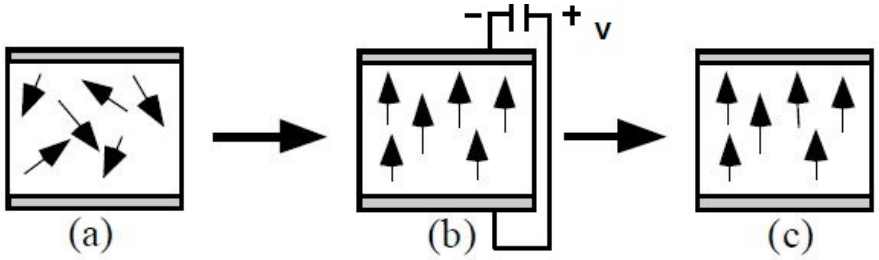

Figure 2-2. Poling process (a) before poling (b) applying direct voltage (c) after poling [8]

To achieve the piezoelectric response, a material must have a crystal structure that lacks a center of symmetry. Twenty of the possible 32 point groups that describe a crystal's symmetry fulfill this requirement and are piezoelectric [8]. Ferroelectric materials after poling process have remnant polarization P_r, and the polarization subject to change which when external stress is applied, it becomes piezoelectric active. Moreover, their piezoelectric response is usually far more significant than other non-ferroelectric piezoelectric crystals.

With direct electroemechanical coupling for piezoelectric materials, the constitutive equations describing the piezoelectric response are shown as follows:

$$S_{ij} = s_{ijkl}^{E}\sigma_{kl} + d_{kij}E_k \qquad (2.1)$$

$$D_i = d_{ikl}\sigma_{kl} + \varepsilon_{ik}^{T}E_k \qquad (2.2)$$

where σ is the mechanical stress (N/m^2), S is the mechanical strain, s is the mechanical compliance (m^2/N), d is the piezoelectric strain coefficient (C/N-m^2), E is the electric field (V/m), D is electric displacement or surface charge density (C/m^2), and ε is the dielectric permittivity (F/m), and substrates i, j, k and l are indices which equal 1 through 3. Equations 2.1 and 2.2 are tensor equations. Strain, stress and dielectric permittivity are second order tensors, piezoelectric coefficient is third order tensor, and elastic compliance is fourth order tensor. A matrix notation is usually used, i.e., 11 → 1; 22 → 2; 33 → 3; 23, 32 → 4; 13, 31 → 5; and 12, 21 → 6 when matrix equations are used to describe the electromechanical constitutive relations.

In matrix form,

$$\{S\} = [s^E]\{T\} + [d^t]\{E\} \tag{2.3a}$$

$$\{D\} = [d^E]\{T\} + [\varepsilon^T]\{E\} \tag{2.3b}$$

Here T is stress.

The strain-charge for a material of the 4mm crystal class (such as a poled piezoelectric ceramic such as tetragonal PZT or $BaTiO_3$) as well as the 6mm crystal class may also be written as[6]:

$$\begin{bmatrix} S_1 \\ S_2 \\ S_3 \\ S_4 \\ S_5 \\ S_6 \end{bmatrix} = \begin{bmatrix} s_{11}^E & s_{12}^E & s_{13}^E & 0 & 0 & 0 \\ s_{21}^E & s_{22}^E & s_{23}^E & 0 & 0 & 0 \\ s_{31}^E & s_{32}^E & s_{33}^E & 0 & 0 & 0 \\ 0 & 0 & 0 & s_{44}^E & 0 & 0 \\ 0 & 0 & 0 & 0 & s_{55}^E & 0 \\ 0 & 0 & 0 & 0 & 0 & s_{66}^E = 2\left(s_{11}^E - s_{12}^E\right) \end{bmatrix} \begin{bmatrix} T_1 \\ T_2 \\ T_3 \\ T_4 \\ T_5 \\ T_6 \end{bmatrix} + \begin{bmatrix} 0 & 0 & d_{31} \\ 0 & 0 & d_{32} \\ 0 & 0 & d_{33} \\ 0 & d_{24} & 0 \\ d_{15} & 0 & 0 \\ 0 & 0 & 0 \end{bmatrix} \begin{bmatrix} E_1 \\ E_2 \\ E_3 \end{bmatrix} \tag{2.4a}$$

$$\begin{bmatrix} D_1 \\ D_2 \\ D_3 \end{bmatrix} = \begin{bmatrix} 0 & 0 & 0 & 0 & d_{15} & 0 \\ 0 & 0 & 0 & d_{24} & 0 & 0 \\ d_{31} & d_{32} & d_{33} & 0 & 0 & 0 \end{bmatrix} \begin{bmatrix} T_1 \\ T_2 \\ T_3 \\ T_4 \\ T_5 \\ T_6 \end{bmatrix} + \begin{bmatrix} \varepsilon_{11} & 0 & 0 \\ 0 & \varepsilon_{22} & 0 \\ 0 & 0 & \varepsilon_{33} \end{bmatrix} \begin{bmatrix} E_1 \\ E_2 \\ E_3 \end{bmatrix} \tag{2.4b}$$

where the first equation represents the relationship for the converse piezoelectric effect and the latter for the direct piezoelectric effect.

The important relation for direct piezoelectric effect that used in pressure sensor is between mechanical stress and charge generation, which is represented as constant *d* [8]. For open-circuit case, the electric field *E* is zero, thus the equation 2.2 becomes:

$$D_i = d_{iJ} T_J \qquad (2.5)$$

where subscript J is from 1 to 6. Equation 2.3 indicates the linear relationship between applied stress and generated electric charge density. It should be noted that the correlation extent between stress and electric displacement is dependent on the piezoelectric coefficient d_{iJ} which is a critical factor for the sensitivity of a piezoelectric pressure sensor. The d_{33} and d_{31} are typically used in force and pressure sensor applications. The d_{33} mode implies that the force or stress is applied across the thickness, and normal to the upper or lower surface of a piezoelectric element along 3-direction (polarization direction), and the charge is collected on the electrodes, whereas the d_{31} mode implies that the direction of applied force or stress is along 1-direction that perpendicular to the direction of polarization and charge collection. The two modes are shown in Figure 2-3

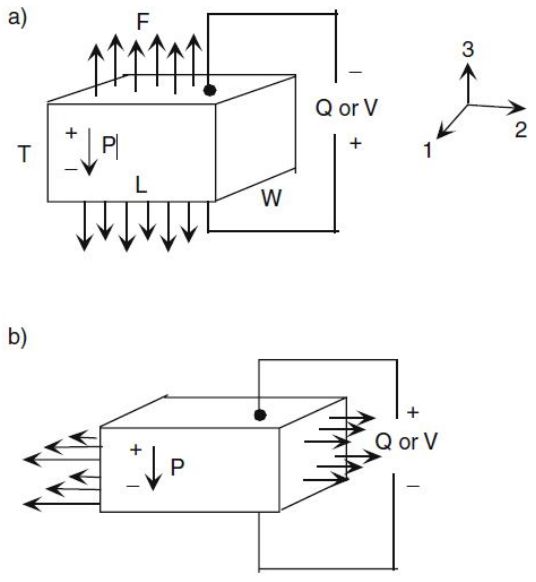

Figure 2-3. Force/Charge relationship on piezoelectric element ;(a) d33 mode; (b)d31 mode [9]

The induced voltage, V, can be derived from equation 2.6a and 2.6b, while the former is for d_{33} mode and the latter for d_{31} mode [8].

$$V_3 = d_{33}.F_3.t/(\varepsilon_{33}.L.W) \qquad (2.6a)$$

$$V_1 = d_{31}.F_3.t/(\varepsilon_{11}.L.t) \qquad (2.6b)$$

where L, W, t are the length, width and thickness of a piezoelectric material, respectively. It can be seen that if an external pressure is applied on the crystal, the voltage generated will be proportional to the pressure. As long as connected in a proper interface, the pressure sensed by piezoelectric material can be obtained as readable data. Based on this mechanism, piezoelectric effect is widely used for industrial sensing applications.

2.2 ADVANTAGES AND DISADVANTAGES OF PIEZOELECTRIC PRESSURE SENSORS

The utilization of piezoelectric effect as the pressure measuring principle has experienced a constant growth and can nowadays be regarded as a mature technology with an outstanding inherent reliability. It has been successfully used in various critical applications as for example in medical, aerospace and nuclear instrumentation [10].

There are several inherent advantages of piezoelectric pressure sensor compared with other mechanisms. First of all is that the high modulus of elasticity of piezoelectric materials is comparable to that of many metals and goes up to (~6.2×10^{10} N/m^2), thus they can produce a high output with very little strain. In other words, piezoelectric sensing elements have essentially no deflection and are often referred to as solid state [11]**.** Therefore piezoelectric sensors are rugged, typically having very high natural frequencies and an excellent linearity over a wide

loading range; it is reported that “when coupled with properly designed signal conditioners, piezoelectric sensors typically have a dynamic amplitude range (i.e., maximum measurement range to noise ratio) on the order of 120dB [11].” In addition, piezoelectric technology is insensitive to electromagnetic fields and radiation, enabling measurements under harsh conditions [10, 11].

The major disadvantage of piezoelectric pressure sensors is that they can only measure dynamic or changing events. It is because a static pressure will result in a fixed amount of charges on the piezoelectric material, causing an initial voltage output. “While working with conventional electronics, imperfect insulating materials, and reduction in internal sensor resistance will result in a constant loss of electrons [11]”, causing the signal slowly decay or drain away and yielding an inaccurate signal output.

Therefore Piezoelectric Pressure Sensors generally are used in measuring dynamic pressures. Dynamic pressure measurements including turbulence, blast, ballistics, and engine combustion under varying conditions may require sensors with special capabilities. Fast response, ruggedness, high stiffness, extended ranges, and the ability to also measure quasi-static pressures are standard features associated with piezoelectric pressure sensors.

2.3 GENERAL STRUCTURES OF PIEZOELECTRIC SENSOR

Generally there are three types of operations for piezoelectric sensors: parallel compression (or tension), flexural (transverse) and shear, as shown in Figure 2-4

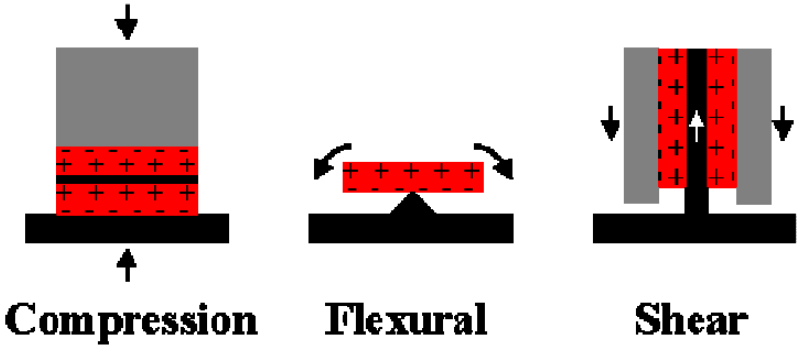

Figure 2-4. Operation modes of piezoelectric sensors [11]

The parallel compression design, which is d_{33} mode that mentioned in former section, features high rigidity, making it useful for implementation in high frequency pressure and force sensors. Its disadvantage is that it is somewhat sensitive to thermal transients, i.e., charge generation due to temperature fluctuation, or pyroelectricity that is inherent to ferroelectric materials. As for the flexural design which operating in d_{31} mode, a force is applied along a transverse axis and the charges are generated along the z-direction. The simplicity of the flexural design is offset by its narrow frequency range and low overshock survivability. And shear structure is typically used in accelerometer for its good balance in different properties such as wide frequency range, low off axis sensitivity, low sensitivity to base strain and low sensitivity to thermal inputs [11].

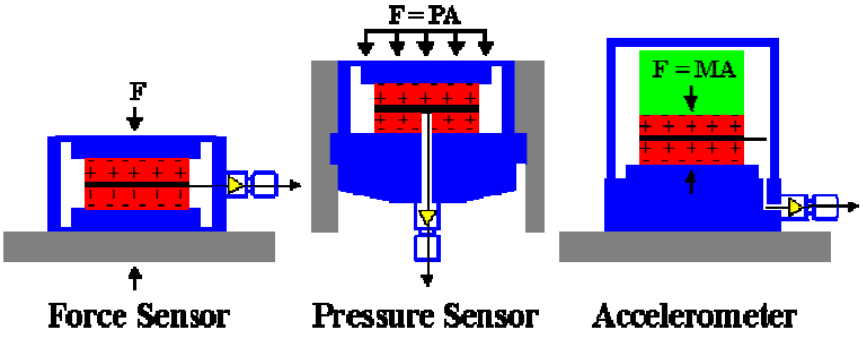

Figure 2-5. Typical force, pressure and acceleration sensor [11]

A representation of a typical force, pressure and acceleration sensor is shown in Figure 2.5. It can be seen that pressure and force sensors are nearly identical and rely on an external force to strain the crystals. To be more sensitive to pressure signals, pressure sensors generally utilize a diaphragm to collect pressure, i.e. the force applied over an area [11].

From Figure 2-5, it can be shown that the different types of piezoelectric sensors are similar in configurations. Therefore, sensors designed to measure one specific parameter are also somewhat suspected by other undesirable inputs. By minimizing their sensitivity to disturbance, sensors can be more accurate to sense intended signal. Commercial pressure sensors often utilize acceleration-compensation and thermal-compensation components to reduce the sensitivity to motion and temperature inputs. And some accelerometers utilize alternative shear-structure sensing elements to reduce the effect of thermal transients, transverse motion and base strain.

In the next section, the piezoelectric element used in pressure sensor applications will be investigated more detailed.

2.4 DIFFERENT TYPES OF PIEZOELECTRIC SENSING ELEMENT

As mentioned in last section, piezoelectric pressure sensors generally utilize a diaphragm to sense pressure. A key processing challenge is to create a piezoelectric diaphragm with the desired dimensions and properties. Approaches based on different piezoelectric materials for pressure sensing are briefly introduced below.

Quartz

Quartz crystals were the first commercially exploited piezoelectric material. There are various excellent properties making quartz suitable for use as a measuring element [12]: 1.High

permissible surface pressure of about 150 N/mm^2 2.Withstands temperatures up to 500 °C. 3. Very high rigidity, high linearity and negligible hysteresis.4. Practically constant sensitivity over a wide temperature range 5.extremely high insulation resistance ($10^{14}\Omega$) allows measurement of low frequencies (<1Hz).

Zinc Oxide

Zinc Oxide (ZnO) is a relatively soft piezoelectric material which has been used in MEMS as surface acoustic wave (SAW) or bulk acoustic wave (BAW) resonators. Its application in pressure-sensing in micro-fluid system was investigated by Kuoni et al (2003). In their study, a ZnO thin film pressure sensor was presented. Piezoelectric ZnO thin film was chosen because it can be deposited onto the polymer membrane without external heating or a seed layer, and its capacity of self-poling is also favorable. Two ZnO sensors were placed on different positions of a flow chamber to measure the liquid pressure difference, thus indicating the flow speed. The piezoelectric coefficient of this ZnO sensor was measured, which is capable to detect nl and sub-nl stroke volumes in micro fluid systems [13].

Aluminum Nitride

Akiyama et al. (2006) reported a flexible piezoelectric pressure sensor using oriented aluminum nitride (AlN) thin films prepared on polyethylene terephthalate (PET) films [14]. Because of the high sensitive piezoelectric response and high thermal and chemical stabilities, AlN is an excellent piezoelectric material in applications of MEMS and bulk acoustic wave devices. The sensor consists of Platinum (Pt) electrode, AlN layer and PET film to obtain sensitivity, flexibility, and fatigue durability. The responses of the sensor in a pressure range

from 0 to 8.5Mpa with a vibration exciter at room temperature are investigated. Another type of AlN pressure sensor fabricated by Akiyama (2003) was used to detect human pulse wave form. This flexible sensor was made from density-packed oriented aluminum nitride nano-columns prepared on aluminum foils.

PVDF Films

PVDF film is a flexible, lightweight, tough engineering plastic available in a wide variety of thicknesses and large areas. Piezoelectric PVDF and its copolymer films have low density and excellent sensitivity, and are mechanically tough. The compliance of PVDF film is 10 times greater than the compliance of ceramics [15]. When extruded into thin film, piezoelectric polymers can be directly attached to a structure without disturbing its mechanical motion. The piezoelectric film is well suited to strain/stress sensing applications requiring very wide bandwidth and high sensitivity. Shirinov et al. (2008) [16] investigated the properties of the pressure sensor made of PVDF that suitable to work in different media. Their design of such a pressure sensor is presented in FigureFigure2.6, which consists of a piezoelectric PVDF film with electrodes deposited on both sides, electric contacts attached to the electrodes, a housing made from PVDF, deflection stop protecting the PVDF film against an overpressure, and a support linearizing the characteristic curve of the sensor. When a pressure change is applied to the sensor, the PVDF pressure film is strained and due to its piezoelectric properties an electric charge are generated on the electrodes. This electric signal is measured with a simple electric circuit. The experiments have shown that the form of the characteristic curve is a function of the sensor design.

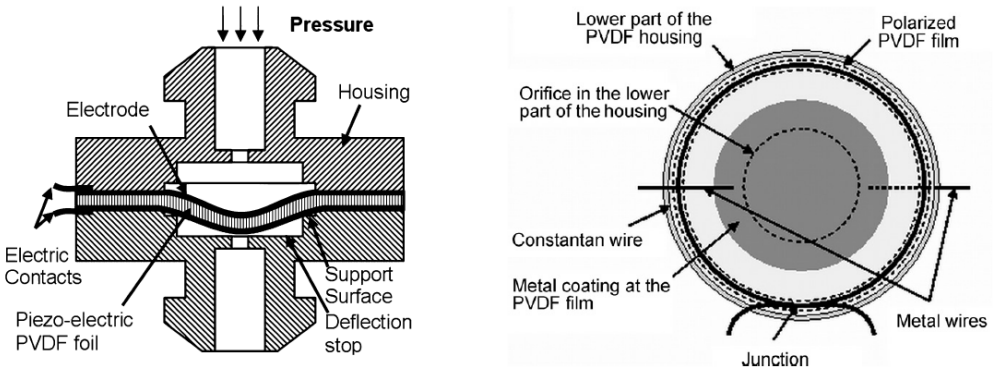

Figure 2-6. Schematic of a PVDF pressure sensor: left: cross-section right: top view [16].

There are a number of practical applications using piezoelectric PVDF pressure or stress sensors. Roberto Marsili (2000) presented an application of PVDF films for the evaluation of the dynamic normal pressure exchanged between the ground and the tire of a moving car [17]. In the study by Akitegetse et al. (2008), PVDF film is used to measure interfacial stress between an ice layer deposited on an aluminum substrate. The small thickness of PVDF as well as its flexibility makes this sensing material an excellent candidate for this task [18]. Another application is introduced by P. de Bruyne (1988) that used for automatic verification of hand-written signatures [19].

3.0 PROPOSAL AND DESIGN OF PZT THICK FILM PRESSURE SENSOR

In previous section, different types of piezoelectric materials as pressure sensing element are reviewed. The research objective in this thesis is to investigate and fabricate a flexible dynamic (or quasi-static) pressure sensor that can withstand relatively large deformation. Therefore this type of pressure sensor can be installed onto curved surfaces such as those in pipeline pressure sensing, human pulse or heart rate monitor. The brittle character of Quartz makes it not feasible to be flexible sensor. PVDF has good flexibility but the piezoelectric charge coefficient is relatively low, and the temperature influence on its sensitivity is relatively high, which is not desirable in pressure sensing. AlN and ZnO are piezoelectric thin film materials primarily used in MEMS and microfluidic sensors, but the deposition of AlN and ZnO films and texture control are relatively difficult compared with PZT, and their piezoelectric coefficients are much lower than PZT (Table 2). Other Piezoelectric materials such as GaAs and SiC are too expensive or too weak in their piezoelectric effect [20]. Among piezoelectric materials, PZT ceramics has the highest piezoelectric coefficient and electrical-mechanical coupling coefficient which are desirable in sensing application, and the fabrication process is simple and less expensive compared with other piezoelectric materials. However, conventional PZT ceramics are brittle and can only withstand very little bending load. Thus the major challenge to use PZT for pressure sensors is the fabricate PZT thick films with some flexibility in bending deflection. Recent development in the fabrication of thick-film PZT ceramic with thickness about several

tens of micrometers using tape-casting processing makes it possible for the design and fabrication of flexible piezoelectric composite pressure sensors [21]. In this thesis, a highly sensitive diaphragm-type PZT thick film pressure sensor for low frequency quasi-static and blast pressure detection under flexural mode is investigated and analyzed. Two experimental setups are constructed to characterize the sensing capability in different loading conditions. And the initial test of this sensor for monitoring human pulse pressure and pulse wave velocity is also demonstrated.

3.1 FABRICATION PROCESS OF PZT THICK-FILM BY TAPE-CASTING

The PZT thick-film used in this study is fabricated using tape-casting processing by Lifeng Qin et al (2009) [21]: The first step is to prepare PZT ceramics with Zr/Ti ratio of 52/48, with additives such as lanthanum oxide and niobium oxide. To form PZT powders with average particle size in the sub-micrometer range, PbO, ZrO_2, and TiO_2 and additives were mixed together by ball billing, and then followed by drying, calcinations and fine vibratory milling. The slip that is prepared for tape-casting contains the ceramic powders, an organic binder, and other organic additives such as plasticizers, dispersants, and deforming agents. Aqueous and nonaqueous solvent systems are both used as binder systems. For aqueous binder system, slurry is prepared by mixing PZT powder (75 to 86 wt %) with deionized water (13 to 124 wt %) and dispersant (1 to 2 wt%), and then followed by milling process. Next, the milled slurry was added to dispersant (33% TRITON-100 solution in de-ionized water) and a wetting agent (33% TRITON CF-10). The milled slurry solution (85%) was then added to ammoniated 5310 and 5320 acrylic resins (7.5wt% each) to form the slip for tape casing. For nonaqueous binder

system, the binder mix formulation consists of 43 wt% binder polymer solution (acrylic resin), 3wt% plasticizer, and 54 wt% solvent (1.1.-trichlorethane). The PZT powders were added with binder mix to form the slip. The following steps are de-airing and casting: the de-aired PZT green tape sheet with appropriate thickness is cast by a customized belt-casting system using a stainless steel belt (Figure 3.1). PZT sheet with various thicknesses (from 10 to 100 μm) have been prepared. After the sheets prepared, they can be cut or punched to desirable shapes and dimensions such as rectangular and circular disks, and followed by high-temperature binder burnout (at about 500°C) and sintering at higher temperature (1250°C to 1300°C) to form the finished PZT thick-film ceramics. Thin silver electrode paste was coated by screen printing on the two sides of thick-film ceramics and sintered at 650°C. The PZT ceramics were then subjected to poling at 3 to 5 kV/mm electrical strength to induce the piezoelectric activity. Figure 3-2 shows photographs of the PZT films with different thicknesses and shapes.

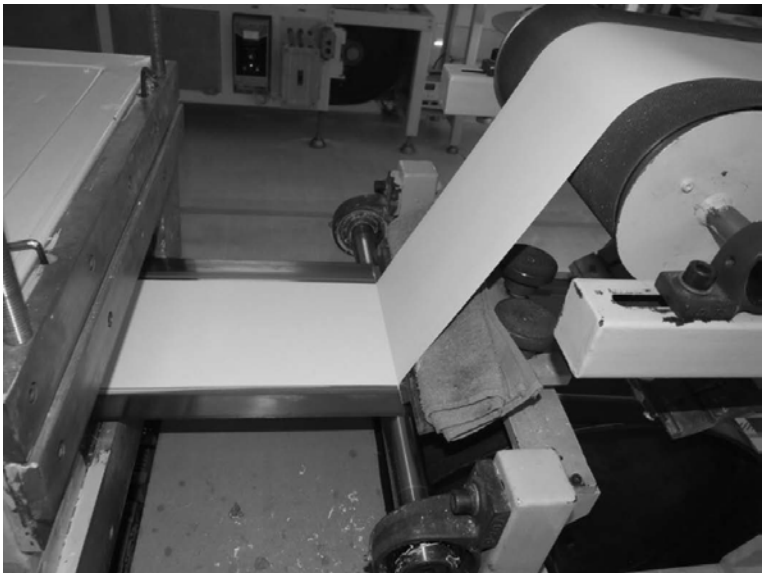

Figure 3-1.PZT green sheet fabricated by the tape-casting processing [21]

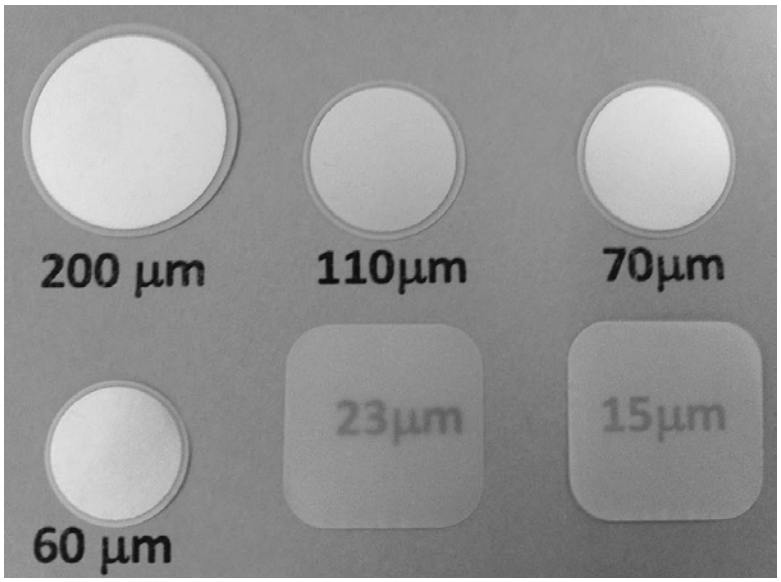

Figure 3-2. The fabricated PZT thick films [21]

3.2 DESIGN AND CONSTRUCTION OF PRESSURE SENSOR

As introduced in Chapter 2, both d_{33} and d_{31} modes are most commonly used for piezoelectric sensor. In d_{33} mode, the mechanical stress is applied along z-direction and directly proportional to the normal force or pressure. Since the objective in the study is to develop and test pressure sensors at for low frequency range and low pressure level applications such as human blood pressure monitoring, of which the pressure is in the range of few kilopascals, it is difficult to achieve high sensitivity for d_{33} mode especially using thick film PZT as sensing element. Higher voltage output can be generated by increasing the thickness of PZT film; however, the flexibility of the sensor will be weakened. As for d_{31} bending mode, the PZT film is stretched or bended due to normal pressure loading, and the stress and strain along radial and transverse direction are much larger than those in normal direction, which results in high sensitivity. For this reason, d_{31} mode will be used in the sensor structure in this study.

3.2.1 Unimorph Structure

The main concept using in the dynamic pressure sensor design is circular diaphragm, which is a common d_{31} structure for pressure sensors with uniform pressure loading applied. As shown in Figure 3.3, a circular PZT thick film is bonded with a metal or polymer substrate. The diameter of substrate is larger than that of PZT, i.e. PZT film is partially covered on the substrate.

Au or Ag electrodes are sputtered on the upper and lower surfaces of PZT film to pick the generated charge. If the boundary of substrate is clamped, when a dynamic uniform pressure normally applied on the lower surface of substrate, the sensor will be deflected and induces charges via d_{31} mode on the PZT film. Supposing the deflection is much smaller than the thickness of sensor plate, based on the small bending elastic theory and piezoelectricity, the output charge (or open circuit voltage) of PZT film should be proportional with the amplitude of applied pressure.

In this thesis, pressure sensor with unimorph structure will be tested using an air blast pressure tube setup, which will be discussed in Chapter 5.

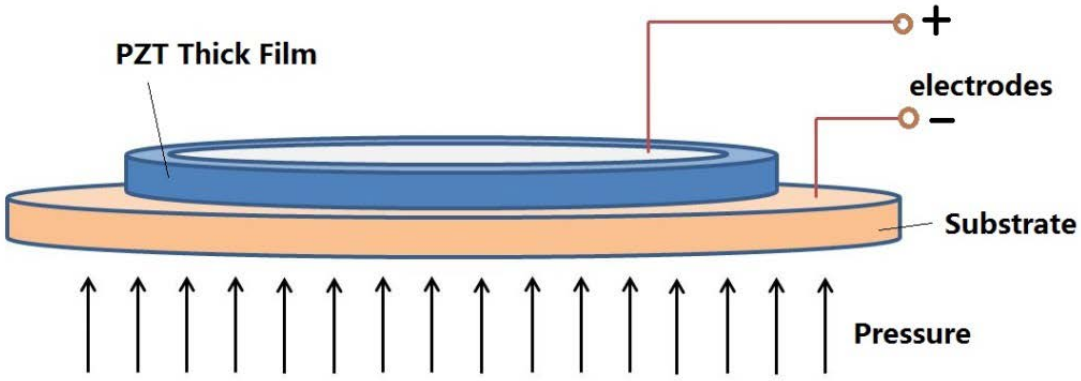

Figure 3-3. Unimorph sensor structure

3.2.2 Sandwiched Composite Structure

Although the PZT thick film used in this study has fairly good flexibility due to its small thickness, but it is also very fragile. Therefore a unimorph structure mentioned in section 3.2.1 will be chosen as a flexible pressure sensor in which a thin non-piezoelectric elastic layer is used as the substrate for PZT layer. With a good flexibility, the unimorph device could be attached onto slightly curved surface and they can be subject to relatively large deflection. When using the device for human body pressure monitoring, the exposure of PZT layer and electrodes may be unfavorable a sandwiched structure can be chosen in that the PZT thick film layer and electrodes can be safely contained in the core between two polymer films. In addition, the bonding process of sandwiched structure often requires elevated temperature up to 200°C to maximize the glue bonding strength, which will result in compressed thermal stress into PZT film and then further increasing its tensile flexibility. The sandwiched structure is shown in Figure 3-4.

In this thesis, sandwiched structure sensor will be tested using a fluid pulse pressure setup, which is discussed in Chapter 4.

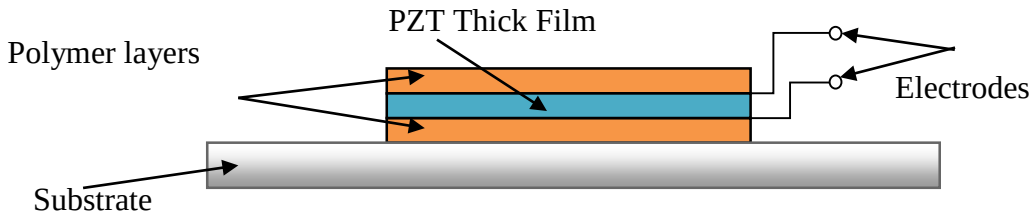

Figure 3-4. Sandwiched Structure

3.3 THEORETICAL ANALYSIS

3.3.1 Static Response

In this section, the theoretical analysis of PZT pressure sensor will be conducted. For simplicity, the mechanical model of sandwiched type is assumed the same as unimorph type, as shown in Figure 3.5. The sandwiched composite is regarded as the 'equivalent piezoelectric layer' and assumed isotropic, the equivalent Young's modulus and Poisson's ratio of this part can be calculated following equation (3.5). Therefore, the unimorph model is applied during analysis.

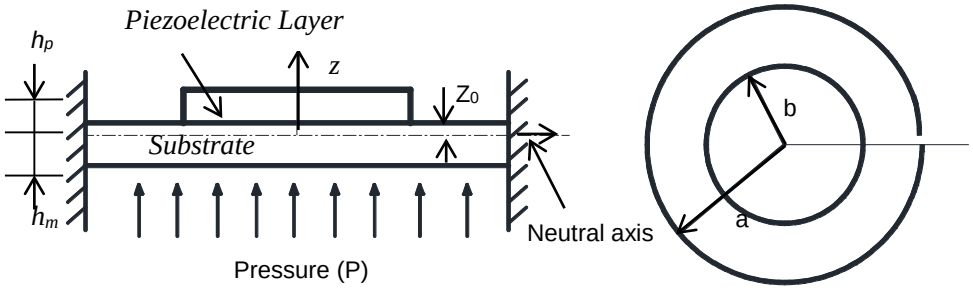

Figure 3-5. Mechanical Modeling of Pressure Sensor

Figure 3.5 shows the mechanical model of the sensor configuration. PZT is assumed to be ideally bonded to substrate, and the substrate is considered fully edge-clamped. h_p and h_m are the thickness of PZT and substrate layer, respectively, a and b the radius of substrate layer and PZT film. Z_o is the distance between interface of two layers (i.e. reference plane) and neutral axis. The effects of both electrodes and bonding layer are neglected. And several additional assumptions are applied for analyzing this problem: 1. No shear strain along the plate. 2. No stress along the z-direction (thickness direction). 3. The deflection is much smaller than the thickness of the plate. In order to calculate the generated charge of PZT subjected to pressure loading, the

electromechanical coupling analysis is conducted, which follows the previous work done by Mo et al (2010) [22] .

First step is to establish the relationship between the deflection of plate and the applied pressure loading. The mechanical model is divided into two parts: the inner part which consists of PZT film and part of metal substrate and outer part which is the annular part of metal substrate, shown as Figure3.6. The deflection of plate in z-direction subjected to normal uniform pressure, the moments and shear force of the plate is given by Vinson (1974) [23]

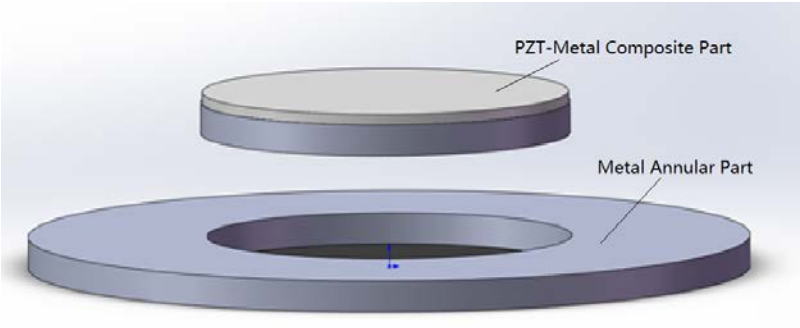

Figure 3-6. Two-part mechanical modeling for convenience of analysis

Deflection of plate in z-direction:

$$\nabla^4 w_i = \frac{1}{r}\frac{\partial}{\partial r}\left(r\frac{\partial}{\partial r}\left(\frac{1}{r}\frac{\partial}{\partial r}\left(\frac{r\partial w}{\partial r}\right)\right)\right) = \frac{P}{D_i} \tag{3.1}$$

Moment in radius direction:

$$M_{ri} = -D_i(w_i'' + \frac{\nu_i}{r}w') \tag{3.2}$$

Moment in angular direction:

$$M_{\theta i} = -D_i(\frac{1}{r}w_i' + \nu w'') \tag{3.3}$$

Shear Force:

$$Q_{ri} = -D_i(\nabla^2 w) = -D_i\frac{\partial}{\partial r}(\frac{1}{r}\frac{\partial}{\partial r}(r\frac{\partial w_r}{\partial r})) \tag{3.4}$$

where w_i can be changed as w_c or w_m, which stands for inner composite part and outer annular metal part, respectively, r is the distance from center of plate, P is the applied pressure and D is the flexural rigidity of plate, $D = (Eh^3) / \left(12(1-\nu^2)\right)$. E is Young's modulus, h the thickness of plate and ν Poisson's ratio. The equivalent Young's modulus E_c and Poisson's ratio of PZT-metal composite part can be derived by following Christensen's work [24]:

$$E_c = C_1E_p + C_2E_m + \frac{C_1C_2E_pE_m(\nu_p - \nu_m)^2}{C_1E_p(1-\nu_m{}^2) + C_2E_m(1-\nu_p{}^2)}$$
$$\nu_c = \frac{C_1\nu_pE_p(1-\nu_m{}^2) + C_2\nu_mE_m(1-\nu_p{}^2)}{C_1E_p(1-\nu_m{}^2) + C_2E_m(1-\nu_p{}^2)} \qquad (3.5)$$

where $C_1=h_p/h$, $C_2=h_m/h$, $h=h_p+h_m$, and subscript $_{c,\,p,\,m}$ indicate composite, PZT and metal part, respectively. Thus the flexural rigidity of each part is given as:

$$D_c = \frac{E_ch^3}{12(1-\nu_c)}$$
$$D_m = \frac{E_mh_m{}^3}{12(1-\nu_m)} \qquad (3.6)$$

The general solution w_i can be derived from equation (3.1)

$$w_m = \frac{pr^4}{64Dm} + \frac{r^2C2}{2} - \frac{r^2C3}{4} + C1lnr + \frac{r^2C3}{2}lnr + c4 \qquad When\ b < r \le a \qquad (3.7)$$

$$w_c = \frac{pr^4}{64Dc} + \frac{r^2C6}{2} - \frac{r^2C7}{4} + C5lnr + \frac{r^2C7}{2}lnr + c8 \qquad When\ 0 \le r \le b \qquad (3.8)$$

There are eight constants C1-C8 which can be determined by boundary and continuity conditions.

The clamped boundary condition is satisfied for this mechanical modeling:

At r=a, $w_i=0$, $dw_i/dr=0$

At center point r=0, due to the finite value $dw_i/dr<\infty$, the constants related to logarithms in w_c, C5 and C7, will be vanished.

The continuity conditions at the interface:

At r=b, $w_c=w_m$, $dw_c / dr=dw_m / dr$; $Q_C=Q_m$, $Mr_c=Mr_m$,

Applying all boundary and continuity conditions into equations (3.7) and (3.8), one can finally get the expressions of w_i:

$$w_m = \frac{pr^4}{64Dm} + \frac{r^2 C2}{2} + C1 lnr + C4 \quad \text{When } b<r<a \tag{3.9}$$

$$w_c = \frac{pr^4}{64Dc} + \frac{r^2 C6}{2} + C8 \quad \text{When } 0\leq r\leq b \tag{3.10}$$

Where C1, C2, C4, C6, C8 can be referred to **Appendix A.**

Next step is to find the relationship between strain, stress and applied pressure loading. The piezoelectric constitutive equation (2.1) and (2.2) for inner composite part can be rewritten in polar coordinate system as following:

$$\begin{aligned} e_{ri} &= s_{11}^E(\sigma_{rp} - \nu_p \sigma_{\theta p}) - d_{31}E_3 \\ e_{\theta i} &= s_{11}^E(\sigma_{\theta p} - \nu_p \sigma_{rp}) - d_{31}E_3 \end{aligned} \tag{3.11}$$

$$D_3 = -d_{31}(\sigma_{rp} + \sigma_{\theta p}) + \varepsilon_{33}^T E_3$$

where e is strain and σ is stress, d_{31} is piezoelectric charge coefficient that induced polarization in direction 3 per unit stress applied in direction 1, E_3 is electric filed strength along z-direction. s_{11}^E is piezoelectric mechanical compliance under constant electric field, $s_{11}^E = 1/E_p$, and ν_p equals $(-s_{12}^E/s_{11}^E)$, D_3 is charge density of piezoelectric layer, and ε_{33}^T is piezoelectric permittivity. The negative sign in front of d_{31} indicates that the polarization direction is downward. Therefore, the stress of inner piezoelectric layer can be expressed as:

$$\begin{aligned} \sigma_{rp} &= \frac{1}{s_{11}^E(1-\nu_p{}^2)}(e_{ri} + \nu_p e_{\theta i} + (1+\nu_p)\,\mathrm{d}_{31}\,E_3) \\ \sigma_{\theta p} &= \frac{1}{s_{11}^E(1-\nu_p{}^2)}(e_{\theta i} + \nu_p e_{ri} + (1+\nu_p)\,\mathrm{d}_{31}\,E_3) \end{aligned} \tag{3.12}$$

And for substrate part, the stress:

$$\sigma_{rm} = \frac{E_m}{(1-\nu_m{}^2)}(e_{ro} + \nu_m e_{\theta o})$$
$$\sigma_{\theta m} = \frac{E_m}{(1-\nu_m{}^2)}(e_{\theta o} + \nu_m e_{ro}) \tag{3.13}$$

The extensional strain e is assumed to be continuous in the layers along thickness direction and governed by curvature κ :

For inner piezoelectric part:
$$e_{ri} = \kappa_{ri}(\mathrm{z}-\mathrm{z}_0)$$
$$e_{\theta i} = \kappa_{\theta i}(\mathrm{z}-\mathrm{z}_0) \tag{3.14}$$

For outer substrate part:
$$e_{ro} = \kappa_{ro}(\mathrm{z}-\mathrm{z}_0)$$
$$e_{\theta o} = \kappa_{\theta o}(\mathrm{z}-\mathrm{z}_0) \tag{3.15}$$

where z is the distance from the interface of two layers. There exist four curvatures $\kappa_{ri}, \kappa_{\theta i}, \kappa_{ro}, \kappa_{r\theta o}$, which can be solved according to moment and strain relationship.

The relationship between moments induced by pressure and stresses in the plate are found to be:

For inner composite part:
$$M_{rc} = \int_0^{h_p} \sigma_{rp}(\mathrm{z}-\mathrm{z}_0)\,\mathrm{dz} + \int_{-h_m}^{0} \sigma_{rm}(\mathrm{z}-\mathrm{z}_0)dz$$
$$M_{\theta c} = \int_0^{h_p} \sigma_{\theta p}(\mathrm{z}-\mathrm{z}_0)\,\mathrm{dz} + \int_{-h_m}^{0} \sigma_{\theta m}(\mathrm{z}-\mathrm{z}_0)dz \tag{3.16}$$

For outer annular part:
$$M_{rm} = \int_{-h_m}^{0} \sigma_{rmo}(\mathrm{z}-\mathrm{z}_0)dz$$
$$M_{\theta m} = \int_{-h_m}^{0} \sigma_{\theta mo}(\mathrm{z}-\mathrm{z}_0)dz \tag{3.17}$$

Substitute (3.8)-(3.11) into (3.12) and (3.13), the curvatures κ can be found as functions in terms of moments (and electric field for piezoelectric layer). According to the equations given by Vinson [23], the relationship between moments and deflection curves are:

$$\begin{aligned} M_r &= -D(w'' + \frac{\nu}{r} w') \\ M_\theta &= -D(\frac{1}{r} w' + \nu w'') \end{aligned} \tag{3.18}$$

By applying this equation into the expressions of curvatures κ, and substituting κ with strains, the strains are finally solved as functions of *z*, *w* (and external electric field E for piezoelectric layer). (Refer to **Appendix A** for the expressions of strains and stresses)

The final step is to use energy method to derive the relationship between generated Charge and applied pressure. The energy density of piezoelectric layer can be described as:

$$dU_p = \frac{1}{2} e_{rp} \sigma_{rp} + \frac{1}{2} e_{\theta p} \sigma_{\theta p} + \frac{1}{2} D_3 E_3 \tag{3.19}$$

Substitute stress terms with strain by equation (3.12), (3.19) can be rewritten as:

$$dU_p = \frac{1}{2} [\frac{1}{s_{11}^E (1-\nu_p{}^2)} (e_{rp}{}^2 + e_{\theta p}{}^2 + 2 e_{rp} e_{\theta p}) - (\frac{2 d_{31}^2}{s_{11}^E (1-\nu_p{}^2)} + \varepsilon_{33}^T) E_3{}^2] \tag{3.20}$$

The energy density of inner metal substrate is

$$dU_{mi} = \frac{1}{2} e_{rp} \sigma_{rmi} + \frac{1}{2} e_{\theta p} \sigma_{\theta mi} \tag{3.21}$$

The energy density of outer metal substrate is

$$dU_{mo} = \frac{1}{2} e_{ro} \sigma_{rmo} + \frac{1}{2} e_{\theta o} \sigma_{\theta mo} \tag{3.22}$$

Once the energy density determined, the total energy can be obtained by volume integration:

$$U_{total} = \int_0^b \int_0^{2\pi} (\int_0^{h_p} (dU_p dz + \int_{-h_m}^{o} dU_{mi} dz) r d\theta dr + \int_b^a \int_0^{2\pi} (\int_{-h_m}^{0} dU_{mo} dz) r d\theta dr \tag{3.23}$$

The integration will result in three terms of *U*, that is,

$$U_{total} = U(P^2) + U(E_3, P) + U(E_3{}^2) \qquad (3.24)$$

The first term donates mechanical strain energy and the third term donates electric potential energy stored in PZT due to its capacitance when subjected to external electric field [22]. The second term is the electromechanically coupling energy, which is needed to build Charge-Pressure relationship. Substituting E_3 with V/h_p, where V is external voltage, and total charge Q can be solved by:

$$Q_{total} = \partial U_{total} / \partial V = [\partial U_p(V, P) + \partial U_p(V^2)] / \partial V \,. \qquad (3.25)$$

Since no external voltage applied, Q is only determined by applied pressure P. The final function between the generated charges (Q_{gen}) of piezoelectric sensor under uniform pressure loading (P) is

$$Q_{gen} = -\frac{3}{4} \frac{a\, b^2 \pi B_3 B_5\, d_{31} D_c h_m (h_m + h_p) s_{11}^E s_m\, (1 + v)}{B_1\, B_6} P \qquad (3.26)$$

The open-circuit capacitance of piezoelectric layer can be determined by

$$C_p = \partial Q_{total} / \partial V = \frac{b^2 \pi\, \varepsilon_{33}^T}{h_p} \left(1 - \frac{2\, K_{31}{}^2\, B_7}{B_1 (1 - v)}\right) \qquad (3.27)$$

Therefore the generated voltage of PZT will be

$$V_{gen} = \frac{Q_{gen}}{C_p} = -\frac{3}{4} \frac{a\, B_3 B_5\, d_{31}\, D_c\, h_m\, h_p\, (h_m + h_p)\, s_{11}^E\, s_m\, (1+v)}{B_6\, B_1\, b^2 \pi\, \varepsilon_{33}^T \left(1 - \frac{2\, K_{31}{}^2\, B_7}{B_1 (1 - v)}\right)} P \qquad (3.28)$$

Therefore, the sensitivity can be expressed as

$$Sensitivity = \frac{V_{gen}}{P} = -\frac{3}{4} \frac{a\, B_3 B_5\, d_{31}\, D_c\, h_m\, h_p\, (h_m + h_p)\, s_{11}^E\, s_m\, (1+v)}{B_6\, B_1\, b^2 \pi\, \varepsilon_{33}^T \left(1 - \frac{2\, K_{31}{}^2\, B_7}{B_1 (1 - v)}\right)} \qquad (3.29)$$

In above equations,

s_m: Elastic compliance of the substrate material, which equals $1/E_m$

ν: Poisson ratio (assuming PZT and metal layer have the same value for simplicity).

K_{31}: Electro-mechanical coupling coefficient which defined as $K_{31}= d_{31} / \sqrt{\varepsilon_{33}^{T} s_{11}^{E}}$.

B_1, B_3, B_4, B_5, B_6, B_7 are structure constants which can be referred to **Appendix A.**

According to equation (3.26)-(3.29), since all other factors are constant, the generated charge Q and voltage are linear functions with respect to input pressure P.

According to equation (3.29), the sensitivity of pressure sensor is determined by the mechanical properties, piezoelectric properties and structure dimensions. By optimizing the substrate material, diameter ratio and thickness ratio of the sensor, highest sensitivity can be achieved.

Figure 3.7 shows the analytical sensitivity performance of the pressure sensors with different thickness ratios and substrate materials. Figure 3.8 shows the Charge-generating performance with different radius ratios. (Parameters are referred to Table 3-1 and material properties sheet [25])

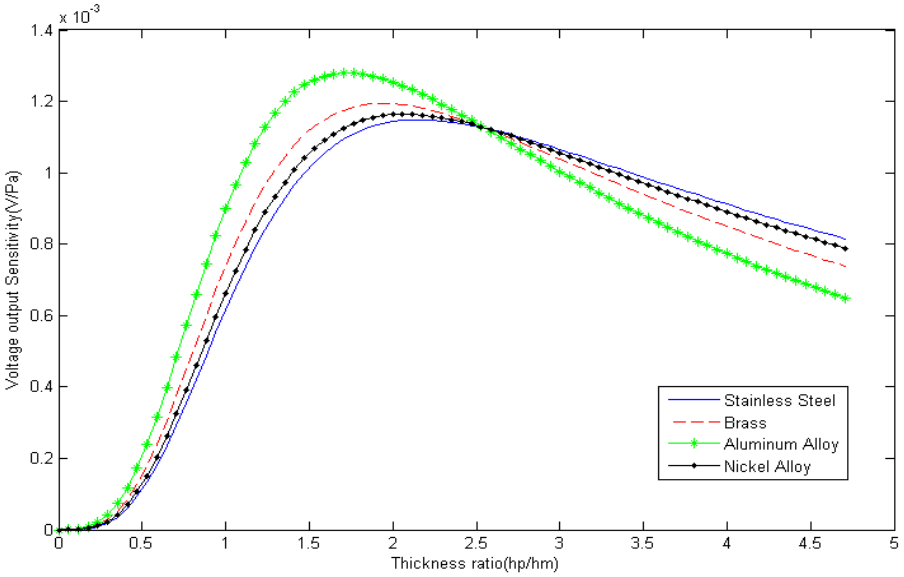

Figure 3-7. Sensitivity performance with different thickness ratios and substrate materials.(b/a=0.6)

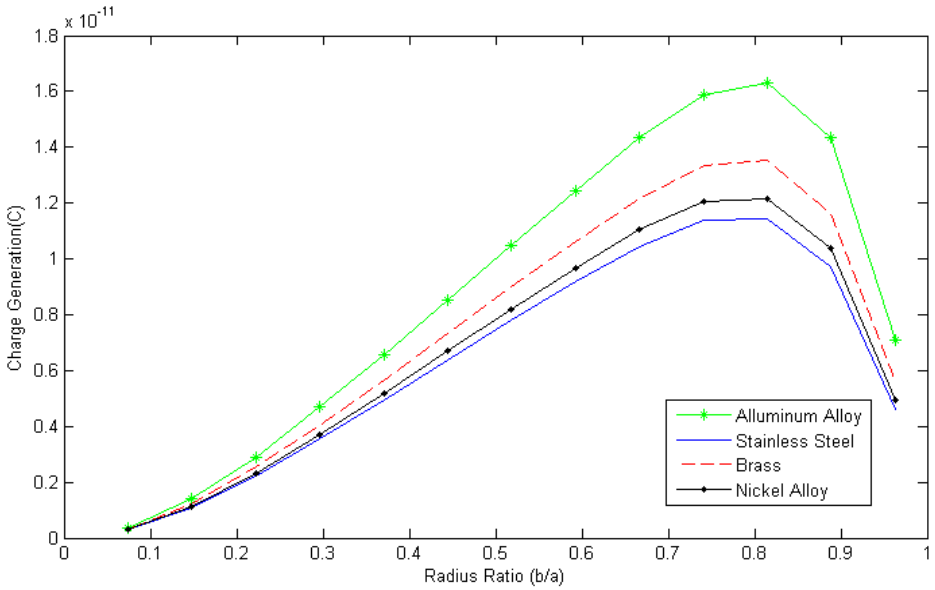

Figure 3-8. Charge-generating performance with different radius ratios and substrate materials.(h_p/h_m=1.5)

According to Figure 3-7 and Figure 3-8, the sensor with aluminum alloy substrate has the highest sensitivity and charge output with a suitable thickness and radius ratio compared with brass, stainless steel and nickel alloy. At a thickness ratio h_p/h_m = 1.75, the pressure sensor will reach to the maximum sensitivity, while at a radius ratio b/a=0.8, the charge output is maximum. Since the optimum thickness ratio varies at different radius ratios, and vice versa, one of them should be determined beforehand when design the sensor dimensions design.

3.3.2 Dynamic Response

A simple mass-damper-spring structure can be used to model the dynamic behavior of the pressure sensor as shown in Figure 3-9a. Assuming a sinusoidal pulsing pressure $P(t) = P\sin\omega t$ applied on the effective surface A, the dynamic equation of the sensor should be:

$$M\ddot{z}(t) + D\dot{z}(t) + Kz(t) = P(t)A \qquad (3.30)$$

Where z (t) is displacement of sensor, *M, D, and K* are effective mass, effective damping coefficient, and effective stiffness, respectively. Applying Laplace transform, equation (3.30) becomes:

$$Ms^2Z + DsZ + KZ = P(s)A \qquad (3.31)$$

Since $s = j\omega$, nature frequency $\omega_n = \sqrt{K/M}$, and $\xi = D/2\sqrt{KM}$, the mechanical transfer function will be:

$$\frac{Z(s)}{P(s)A} = \frac{1}{K}\frac{\omega_n^2}{s^2 + 2\xi\omega_n s + \omega_n^2} \qquad (3.32)$$

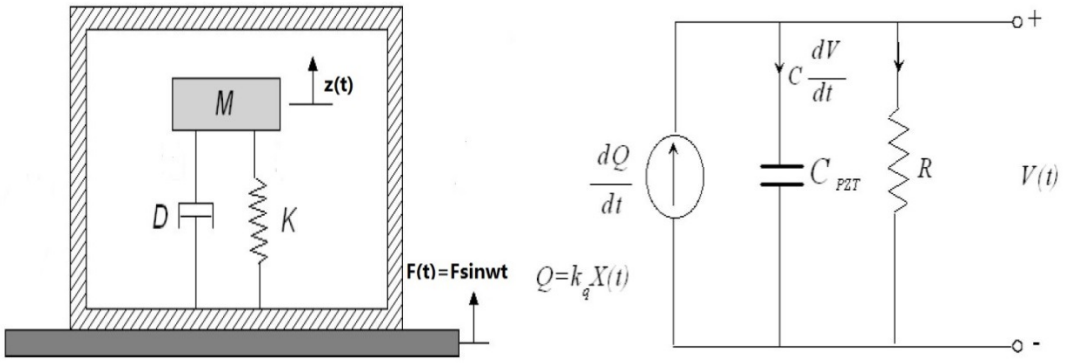

Figure 3-9. (a) Mechanical model of sensor (b) Electrical model of sensor [27]

For the electrical model, the equivalent circuit of pressure sensor is shown in Figure 3-9b, which consist of a charge source *Q (t)*, a leakage resistance R_p, and a dielectric capacitance C_p. the $Q(t) = K_qZ(t)$, where K_q is defined as generated charge per unit center displacement. K_q can be determined by combining equation (3.10) and (3.28) to derive the function of *Q* in terms of center deflection of PZT *w(r=0)*. The expression of K_q is omitted here for simplicity.

Therefore equation (3.32) becomes:

$$\frac{Q(s)}{P(s)A} = \frac{K_q}{K} \frac{\omega_n^{\,2}}{s^2 + 2\xi\omega_n s + \omega_n^{\,2}} \tag{3.33}$$

Using Kirchhoff's current law, the governing equation of the circuit model is:

$$\frac{dQ}{dt} = \frac{K_q dZ}{dt} = C_p \frac{dV}{dt} + \frac{V}{R_p} \tag{3.34}$$

Applying Laplace transform and time constant $\tau = R_p C_p$:

$$\begin{aligned} \frac{K_q}{C_p} sZ(s) &= sV(s) + \frac{V(s)}{\tau} \\ \frac{V(s)}{Z(s)} &= \frac{K_q}{C_p} \frac{\tau s}{\tau s + 1} \end{aligned} \tag{3.35}$$

Substituting (3.35) into (3.33), one could finally get the dynamic equation of the generated voltage vs. applied pressure:

$$\frac{V(s)}{P(s)} = \frac{AK_q}{C_p K} \frac{\omega_n^{\,2}}{s^2 + 2\xi\omega_n s + \omega_n^{\,2}} \frac{\tau s}{\tau s + 1} \tag{3.36}$$

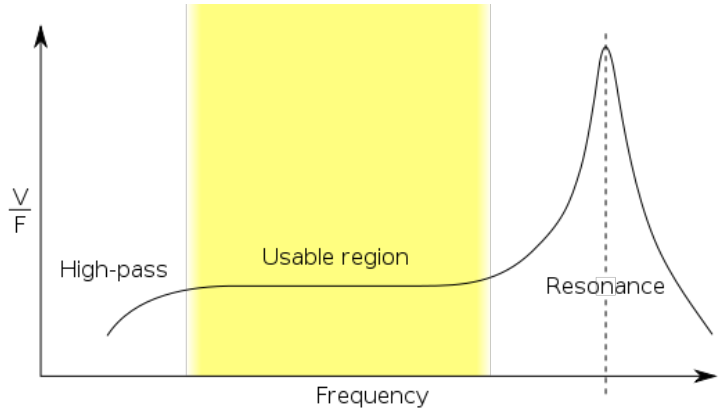

Figure 3-10. Frequency response of a piezoelectric sensor; output voltage vs applied force [28]

The sensitivity curve of the pressure sensor as a function of frequency is shown in Figure 3-10. The useable region refers the frequency-independent flat segment of the curve, in which

the sensitivity of sensor remains constant. The lower limit f_{LL} of the frequency-independent segment curve depends on the leakage resistance R_p and dielectric capacitance C_p of PZT: $f_{LL} = 1/2\pi R_p C_p$.If the load frequency is lower than f_{LL}, the signal amplitude will greatly reduce, resulting in large measurement error. Using $R_p = \rho h_p / A$ and $C_p = \varepsilon A / h_p$ for the PZT layer with resistivity ρ , permittivity ε , thickness h_p and area A, the time constant becomes $\tau = \varepsilon\rho$, which is determined only by piezoelectric PZT material property. The upper limit f_{UL} is the resonant frequency of sensor, which determined by the mechanical properties and structure of sensor.

3.4 FABRICATION PROCESS OF SANDWICHED STRUCTURE PRESSURE SENSOR

In this study, PZT thick films with thickness 70 μm (shown in Figure 3.2) are selected as the sensor sample. The fabrication process includes following steps:

a) First, trim Polyimide films (DuPont Kapton HN) with 75μm thickness as desired circular shape, using a manual hole-punch tool. Then clean up the surfaces of films using ultrasonic cleaner.

b) Secondly, golden electrodes are coated onto these polyimide films using 108-auto sputter coating system (Cressington, Watford, England). A small slot at the edge of the circular film is cut off for electrical contact.

c) Thirdly, uniformly spin coat Polyimide resin (HD MicroSystems P12611) onto one side of Polyimide film, then carefully place PZT film on the top of it. Place another spin coated

polyimide film on the PZT. These three layers should be placed appropriately so that their center point overlapped.

d) Next, sandwich the three layer laminate between two glass plates to ensure the flatness during bonding process, followed by soft-bake in oven (47900 Furnace, Barnstead Thermolyne) at temperature of 140°C. Keep the laminate sandwiched between the two glass plates until the polyimide fully cured. Then take out the samples from oven, and let it cooled down to room temperature. At room temperature, the laminates should be pre-stressed due to thermal effect.

e) Finally, bond the sandwiched laminate on the flexible circular stainless steel layer using epoxy (Eccobond 45 Clear, Ellsworth Adhesives, Germantown, WI). Thin flexible stainless steel was selected due to that it is more robust than other type of flexible materials, such as aluminum or polyimide [29].

Another alternative material, polyimide tape with adhesive coating, is also used in the device fabrication, which can directly bond PZT film into sandwich structure without resin and heat treatment.

Three samples are shown in Figure 3.6. Sample A and B were fabricated using polyimide films (Type I). While sample C used polyimide tape rather than thermal-bonded polyimide films (Type II), thus the thermal pre-stress may be less than the two other samples.

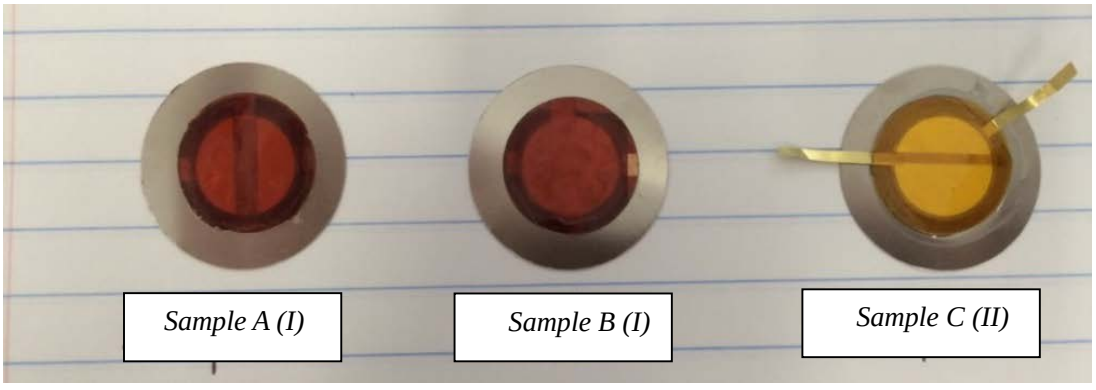

Figure 3-11. Pressure Sensor sample

The properties of PZT and other parameters of the sensor are shown in Table 3-1:

Table 3-1 Properties of pressure sensor sample

Parameters	**Value**
$\varepsilon_{33}^{T} / \varepsilon_{0}$	1527
s_{11}^{E} ($\times 10^{-11}$m^2/N)	2.271
-d_{31}($\times 10^{-12}$C/N)	192
K_{31}	0.347
ν	0.344
$E_{polyimide}$(GPa)	2.5
E_{metal}(GPa)	210
h_{pzt} (mm)	0.07
d_{pzt} (mm)	15
$h_{polyimide}$ (mm)	0.075
$d_{polyimide}$ (mm)	16
h_{metal} (mm)	0.17
d_{metal}(mm)	27

(d=diameter of layer, h=thickness of layer)

4.0 PULSE PRESSURE MEASUREMENT

4.1 EXPERIMENTAL SETUP DESIGN

In order to test the pressure response of the proposed sensor, a measurement setup was designed as shown in Figure 4.1, which consists of two parallel acrylic plates, in which a spindle-like flow channel, a sensor mounting port, an inlet port and outlet port are formed. These two plates are holed together using ten bolts, and O-ring places between them to prevent liquid leakage. In the center of upper cover plate, a circular hole was machined to form the sensor mounting port; the pressure sensor can be edge-clamped on the port using epoxy. The upper surface (sandwiched composite) is exposed to air while the other surface (metal substrate) is exposed to flowing liquid. The flow channel, inlet port and outlet port are formed in the lower plate.

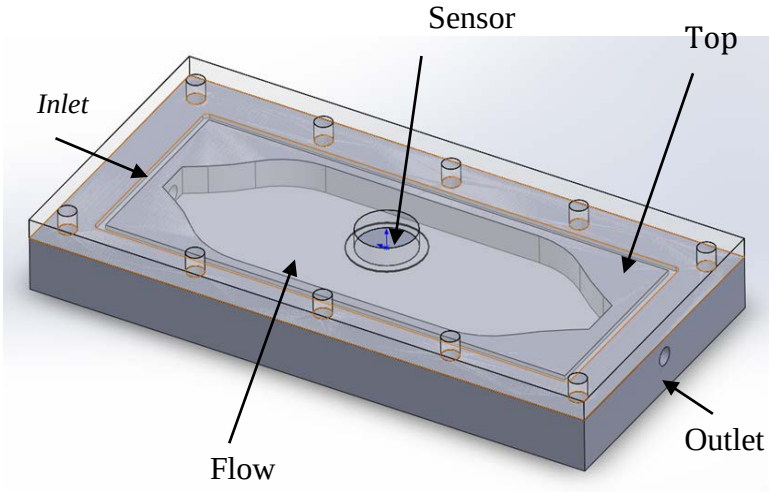

Figure 4-1. Flow chamber

In order to generate dynamic or quasi-static pressure load, a peristaltic pump (Manostat Preston, Thermo Scientific, Barrington, IL) was used (Figure 4.2). A peristaltic pump is a type of positive displacement pump used for pumping a variety of fluids [29], which uses a rotating motor with several rollers (or “wipers”) to compress the soft tube, forcing the fluid to be pumped and pulsed to move through the tube. The operation principle is very similar with many biological systems such as heart beating and gastrointestinal tract. Due to its pulsating nature (particularly at low pump speeds) and controllable flow speed, this peristaltic pump is feasible to generate dynamic pressure and quasi-static load.

Figure 4-2. Peristaltic Pump

When flowing liquid is pumped into the flow chamber through inlet port, the fluid pressure P may consist of two components: static pressure P_o and dynamic pressure P_Δ. That is, $P_t = P_0 + P_\Delta$. The static part, $P_{o,}$ drives fluid moving forward and has a linear relationship with volumetric flow rate Q. The pressure on the pipe wall decreases linearly towards the exit. However, at certain flow speed (i.e. pump rotating speed), the magnitude of P_o is constant and thus has no dynamic effect on the piezoelectric pressure sensor. The dynamic part, $P_{\Delta,}$ is result

from the peristalsis motion of the pump, which causes the pipe wall to be subjected normal pulsating loading. This fluctuating pressure thus can be detected by the flexural pressure sensor mounted at the sensor port. Note that although the shear stress exists along the sensor surface, it is much less than the normal pressure and thus can be ignored.

The pulsating pressure deforms the surface of the sensor and the generated charge signal is then fed into a dual mode charge amplifier (Kistler, type 5010) to convert high impedance charge input to voltage output. The voltage signal from the amplifier will be transferred to an Oscilloscope (DSO-X 4024A, Agilent Technologies) to record the experimental data.

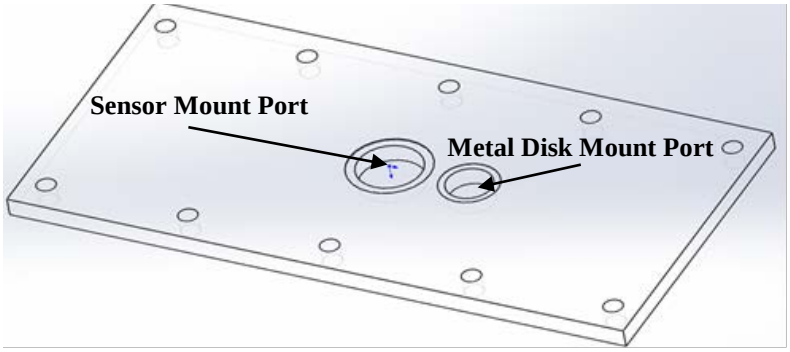

Figure 4-3. Sensor mount hole and metal disk mount hole

While the pressure sensor will convert the dynamic pressure component to electrical output directly, the experimental setup and non-ideal sensor mounting/clamping may introduce error in the pressure measurement. To calibrate the actual dynamic pressure the sensor is subjected to during test, as shown in Figure 4-3, another smaller hole is introduced on the upper plate of the chamber, which is close to the sensor mount port. A circular metal disk (copper) with uniform thickness is placed on the hole with edge clamped using epoxy. Since the distance between two holes is small, it is assumed that the fluctuating pressure on the lower surface of both sensor and the metal disk are equal. Based on the small bending theory of plate, the normal

positive deflection of the center w_r of the metal disk is proportional to the applied pressure P. Since the dynamic pressure causes the disk deflection along normal direction, the peak displacement of the disk center can be detected by a fiber optic vibrometer (MTI 2000 FOTONIC SENSOR). And the relationship between w_r and P is given as follows [23]:

$$w_r = \frac{P}{64D} R^4 \qquad (4.1)$$

Where R is the radius of disk and $D = (Eh_r^3) / \left(12(1-\nu^2)\right)$ is the rigidity of the metal disk, E is the Young's modules, h_r the thickness and ν the Poisson's ratio. Therefore, by measuring the center deflection of the disk, the fluctuating fluid pressure can be calculated and the pressure values can be compared with the voltage values obtained from piezoelectric sensor, simultaneously.

Illustrations of experiment setup are shown in Figure 4-4

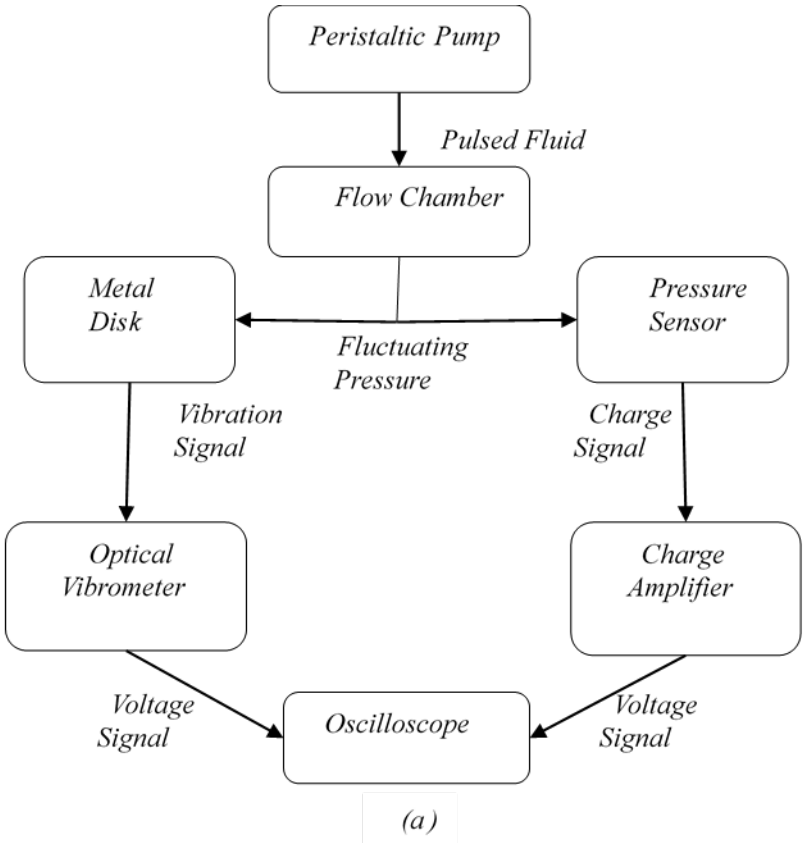

(a)

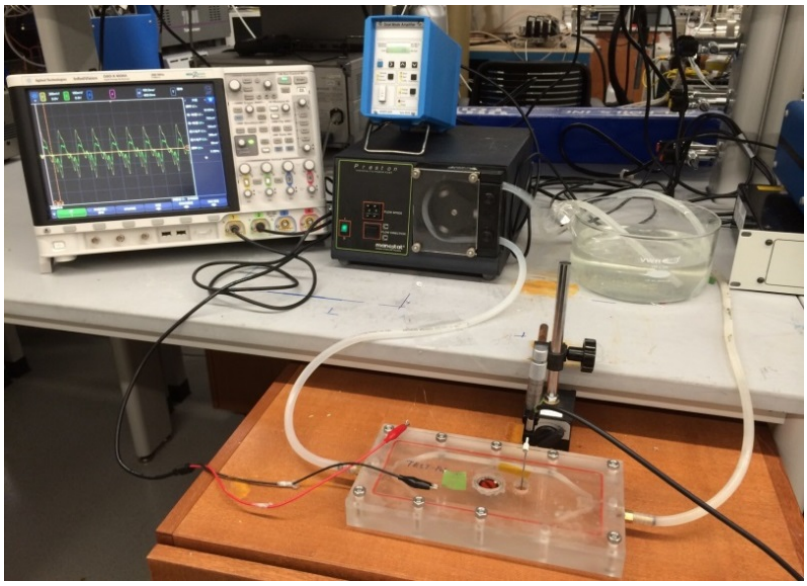

(b)

Figure 4-4. Illustration of experiment setup (a) Measurement setup block diagram; (b) experimental setup

4.2 EXPERIMENTAL PROCEDURE AND RESULTS

The relationship between pump speed and fluctuating pressure applied on the sensor location was firstly investigated. A copper disk with 15mm in diameter and 0.15mm in thickness was bonded on the mount port using epoxy. The probe of optic vibrometer was placed above the center of the disk. By changing the pumping speed, the fluid pressure changes, as well as the zero to peak amplitude of disk center deflection, which is shown in Table 4-1.

Table 4-1 Pump Speed vs. Center deflection of Disk

Pump Speed (mL/s)	**Center deflection (um)**
6	1.28
7	3.04
8	3.68
9	6.88

Table 4-1 (Continued)

Pump Speed (mL/s)	**Center deflection (um)**
10	8
11	5.44
12	5.44
13	5.44
14	6.88
15	10.08
16	9.76
17	8.16
18	7.2
19	7.2
20	8.48
21	9.28
22	10.56
23	12
24	13.28
25	15.36
26	16.8
27	15.36
28	12.96
29	10.88
30	9.28

By applying equation 4.1 with E= 117 GPa and ν =0.335, the relationship of pump speed vs the pulse pressure applied on the copper disk can be obtained, which is shown in Figure 4-5

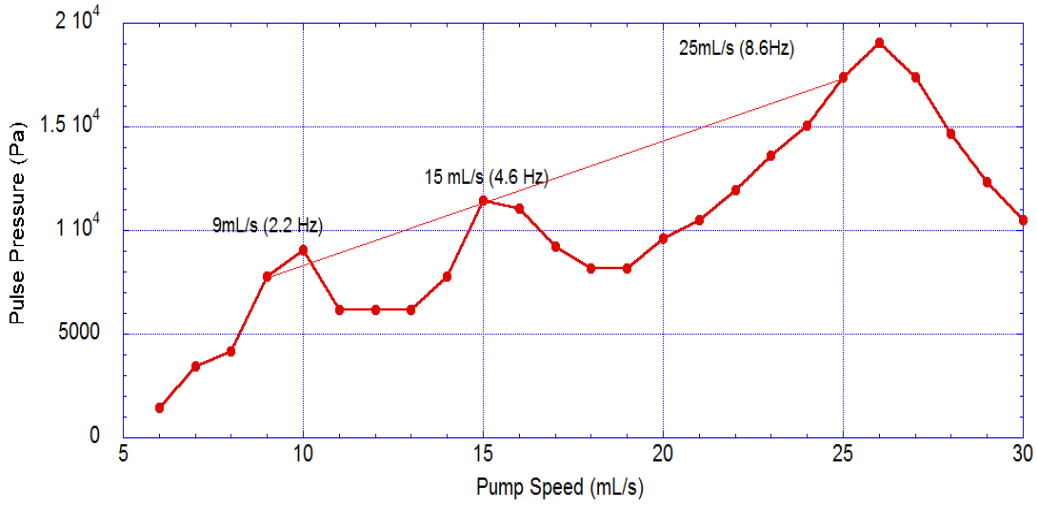

Figure 4-5. The relationship between pump speeds and pulsate pressure

It can be noted that the pulse pressure does not change linearly with the pump speeds. Although increasing pump speeds will correspondingly speed up the average flow rate, which means the static component P_0 will increase proportionally, the factors affect dynamic pressure component P_Δ are more complex. The magnitude of the output pulse pressure from pump relates to the roller numbers and pump occlusion, which are fixed for a certain pump, but during its propagation along the tube and chamber, it is also affected by the rigidity of tube, chamber shape and the disturbance of other noise waves, making the pulse pressure magnitude fluctuate with the change of pump speed. This phenomenon is particularly obvious in low pump speed (low pulse frequency range) [30]. As the pump head rotating in high speed, the flow tends to be steady and the pulsating would be weakened. In order to control variables in the experiment, different pressure amplitudes should be tested under certain pulse frequency. This requirement can be achieved by adjusting the tube clamping screw on the pump. On the other hand, some other factors may also affect the measurement consistency, such as the relative position of test equipment and the ambient vibration. These imperfections of measurement setup may result in

large measurement errors. However, by measuring the pressure both in piezoelectric sensor and optic vibrometer at the same time, these errors can be greatly reduced.

The responses of both the piezoelectric pressure sensor and copper disk under certain pulsed pressure were obtained by charge amplifier and optic vibrometer, respectively. The peak voltages were measured and compared by the two-channel oscilloscope. For example, the voltage output of a pressure sensor sample and the deflection of copper disk in response to several pump speeds were shown in Figure 4-6(a)-(d). The frequency accuracy of the pressure sensor was validated by comparing the measured waveform data with the numbers shown on pump display panel.

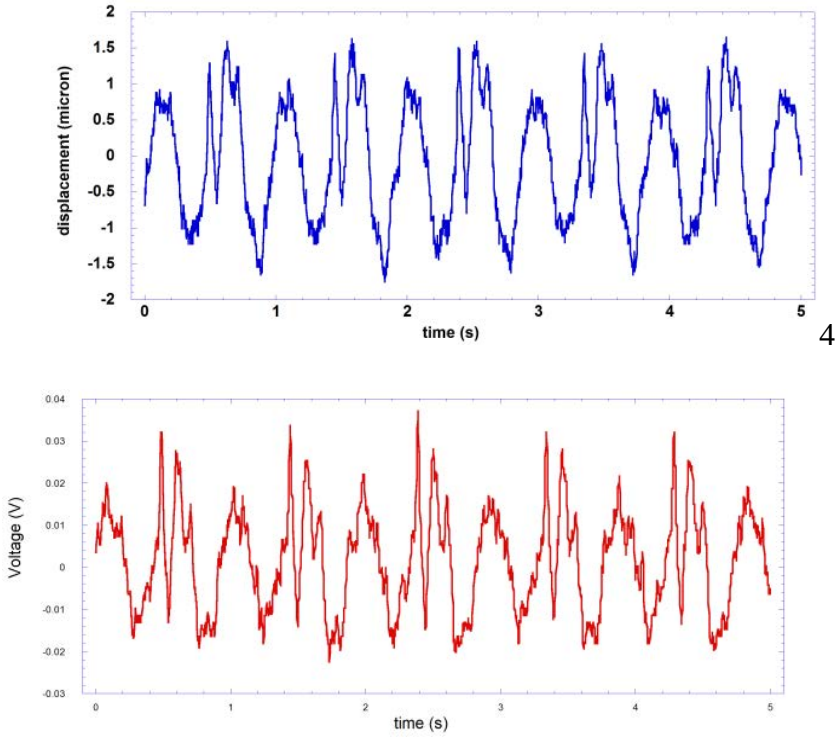

(a) Pump speed 6mL/s (0.97Hz)

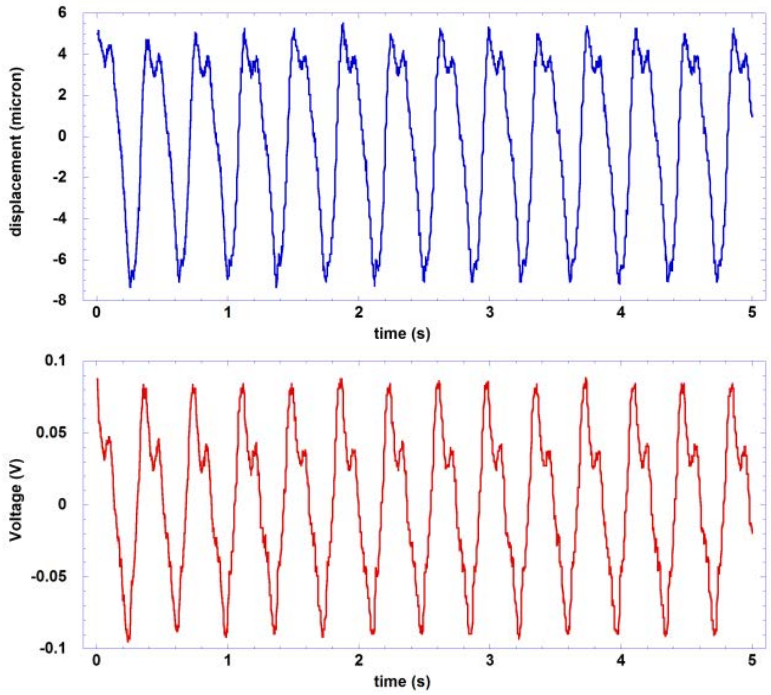

(b) Pump speed 10mL/s (pulse frequency=2.2Hz)

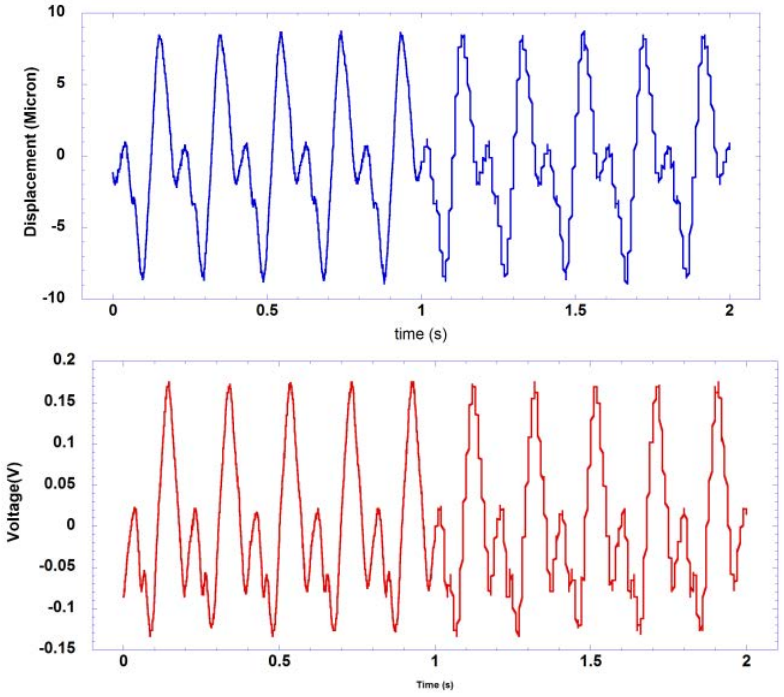

(c) Pump speed 16 mL/s (pulse frequency=4.6Hz)

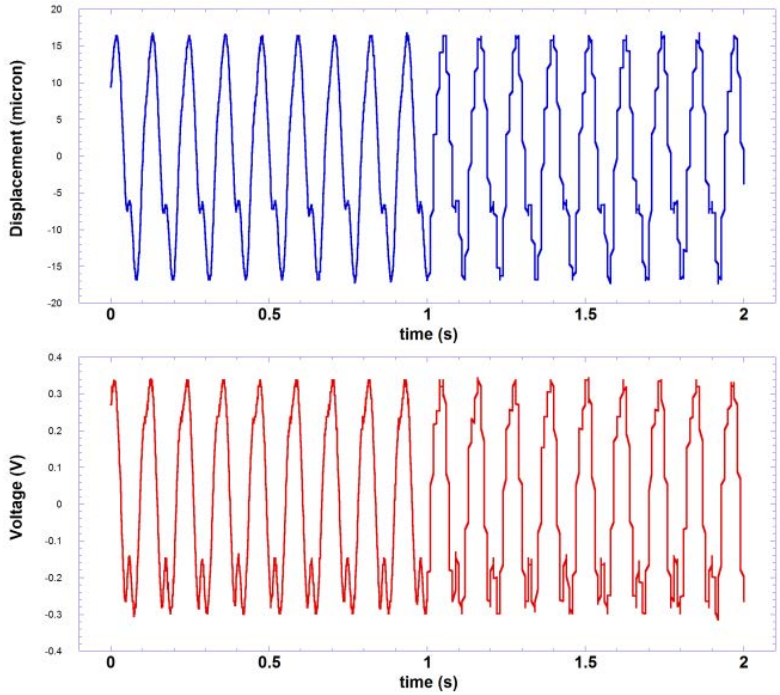

(d) Pump Speed 25 mL/s (pulse frequency=8.6Hz)

Figure 4-6. The pulse pressure responses comparison: Upper: the deflection of copper disk. Lower: the voltage output of piezoelectric sensor

Clearly, the pressure pulse wave that the sensor is subjected to is not a simple sinusoidal wave, fluid turbulence also affect sensor response wave form. At certain pump speed, the pulse amplitude was regulated by adjusting the screw on the pump retainer clamp. Table 4-2 records the sensor responses for pulse pressure sample A at different pulse frequencies, compared with the deflection of copper disk. Since the pressure sensor was designed to detect low pressure at low frequency range, and the small bending elasticity theory applied, the measurement range was limited in few kilopascals. Suppose the linear deflection limit of the copper disk is 1/10 of its thickness, i.e., 0.015mm, the corresponding pressure is about 17 KPa according Equation 4.1. Pump speed at 9ml/s, 15ml/s and 25ml/s are thus selected to test low, medium and high frequency conditions, respectively. The resonant frequencies of sensor samples (installed on the

mount port) were measured by an Impedance Analyzer (Agilent 4294A Impedance Analyzer), which are in the range from 960Hz to 1040Hz. Since the frequencies of input pressure are much less than ten Hz, it can be regarded as quasi-static measurement.

Table 4-2 output voltage vs. disk deflection under certain pulse frequencies

Pump Speed :9mL/s (Pulse Frequency: 2.2Hz)	
*Deflection (**um**)*	*Output Voltage (mV)*
2.4	*67*
2.88	*80*
3.52	*97*
3.68	*105*
4	*114*
4.48	*117*
4.8	*129*
5.12	*136*
5.28	*139*
5.76	*154*
Pump Speed :15mL/s (Pulse Frequency: 4.6Hz)	
*Deflection (**um**)*	*Output Voltage (mV)*
3.2	*67*
4.32	*94*
5.28	*107*
7.52	*147*
8.64	*187*
9.6	*201*
10.72	*221*
11.84	*241*
12.8	*268*
13.92	*274*

Table 4-2 (Continued)

Pump Speed :25mL/s (Pulse Frequency: 8.6Hz)	
*Deflection (**um**)*	*Output Voltage (mV)*
7.52	*161*
8.64	*174*
9.12	*184*
10.24	*228*
11.84	*261*
12.8	*281*
13.92	*301*
15.04	*348*

The peak values of copper disk deflection were converted to pressure values and the relationship between peak pressure and peak voltage was built. The characteristic curves of the piezoelectric sensor at different pulse frequencies shown in Figure 4-7.

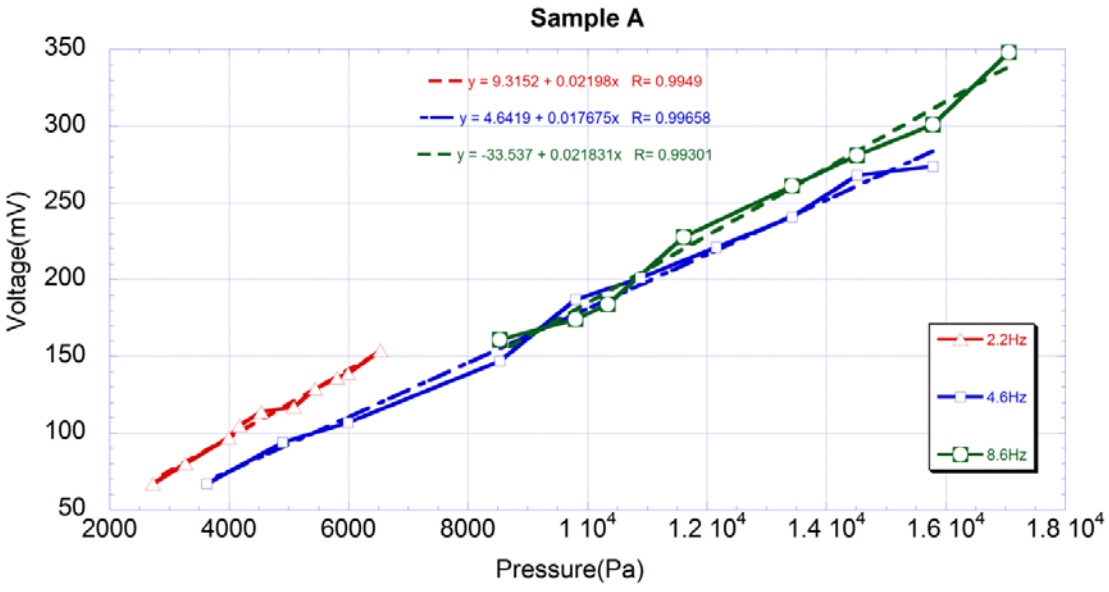

Figure 4-7. Characteristic Curves of Sample A

The voltage-pressure relationships in Figure 4.7 were fitted by least square approximation: V=9.3152+0.02198P, V=4.6419+0.017675P, V=-33.537+0.021831P for pulse frequency at 2.2HZ, 4.6Hz, 8.6Hz, respectively. The sensitivity of sensor can be calculated from the slope of fit lines. Note that the transducer sensitivity of Charge Amplifier was set to 3000pC/MU, and the scale 20MU/V was used, which means 60000pC can generate 1V output voltage on the oscilloscope. The capacitance of piezoelectric film was 28nF measured by Agilent 4294A Impedance Analyzer. So the sensitivity of this sample A in each frequency is 47.1, 37.9, and 46.8 (mV/KPa).

Sample C was also tested in the similar way. The results were shown in Figure 4.8.

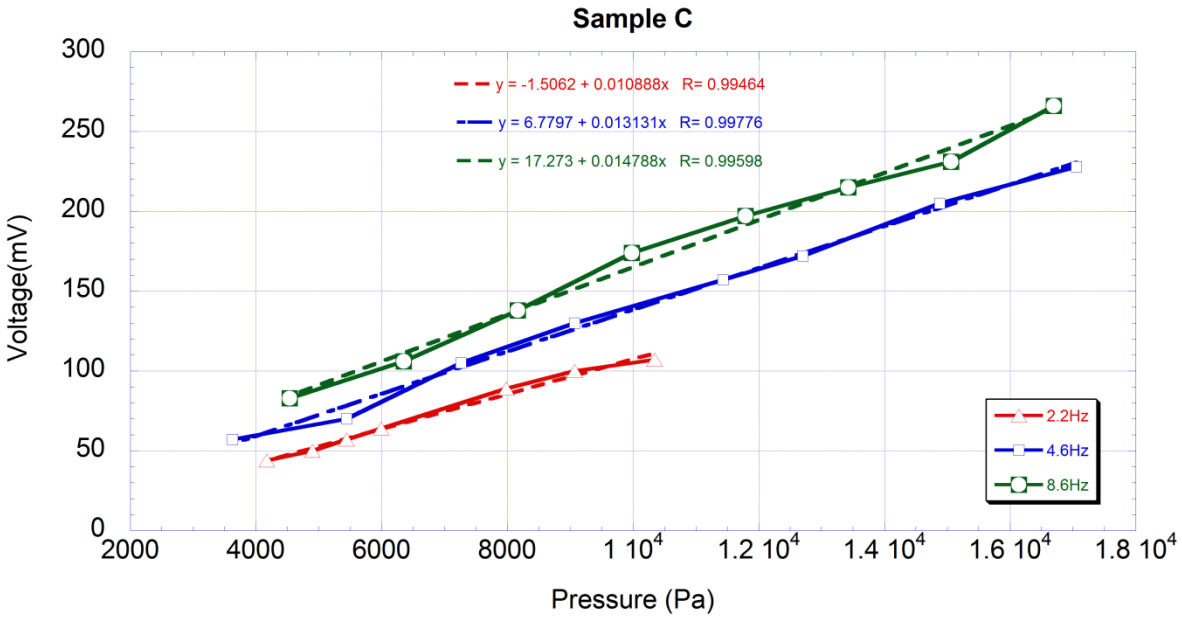

Figure 4-8. Characteristic Curves of Sample C

The voltage-pressure relationships in Figure 4.8 were fitted as: V=-1.5062+0.010888P, V=6.7797+0.013131P, V=17.273+0.014788P for pulse frequency at 2.2Hz, 4.6Hz, 8.6Hz, respectively. The capacitance of piezoelectric film was 25nF. So the sensitivity of sample C is about 23.3, 28.1, and 31.7(mV/KPa).

Table 4-3 compares the experimental results of sensitivity with the theoretical sensitivity, which are calculated from Equation 3.28. The experimental sensitivity of sample A at pulse frequency 2.2 Hz and 8.6Hz agree well with the theoretical value, while others are below.

Table 4-3 Comparison of Experiment and Theoretical Sensitivities

Sensor Model	Sensitivity(mV/KPa)		
	2.2Hz	4.6Hz	8.6Hz
Sample A	47.1	37.9	46.8
Sample C	23.3	28.1	31.7
Theoretical Value	43.328		

4.3 ANALYSIS AND DISCUSSION

The pressure sensor samples exhibited good linearity of voltage-pressure relationship at certain pulse frequency. Sensor sensitivity could be improved by optimizing the thickness and radius ratio between piezoelectric and substrate layers which discussed in Section 3.3. More samples with different dimensions should be fabricated and tested in the future work. The sensitivity of each sensor sample has slight deviations at different pulse frequencies and the values are below theoretical result. Several reasons may result in this inconsistence.

The first possible reason is the dynamic effect of frequency response. As discussed in section 3.3. For a dynamic piezo pressure sensor, the sensitivity depends on frequency. The effective sensitivity is typically measured at the flat segment of the frequency-independent curve. The lower limit f_{LL} of the frequency-independent segment curve depends on the leakage resistance R_p and dielectric capacitance C_p of PZT. However, the time constants of PZT samples

used in our study are typically larger than 1000s, so the lower limit frequency should be less than 0.0001 Hz. This frequency limit is much lower than the frequencies of pulse pressures tested in our experiment, thus this quasi-static measurement still operates in the frequency-independence range. Therefore, the dynamic frequency response has little influence on the sensitivity deviation.

The second possible reason may come from the turbulence of fluid in the chamber. When the pulsed fluid enters the chamber, the pulse wave will not only propagate forward, but also impact on the boundary and corner of the chamber. The reflected pulse wave may cause difference on the prime pulse wave at the sensor mount position and copper disk position, even though they close to each other. At various pulse frequencies, this disturbance is different due to the phase difference between prime wave and reflected wave at these two positions, making the superposed amplitude of pressure waves vary. Therefore the structure of chamber should be modified in the future work. The mount positions of sensor and copper disk should be machined symmetrically on the upper and lower chamber wall, thus the disturbance of noise wave can be minimized.

Another reason is due to the measurement method for the pressure applied on the copper disk. The optic vibrometer is very susceptible to the environment noise, including the vibration of pump, water tube, chamber and the base of the vibrometer, which varies at different pulse frequencies. All of these noises account for the output vibration signal of the copper disk, but have little effect on the output voltage signal of piezoelectric sensor. According to our experiment method, the amplitudes of pressure are converted from the vibration magnitudes of disk. Therefore the sensitivities of piezoelectric to the disk deflection will fluctuate. The method

to calibrate pressure amplitude should be optimized in the future work; a standard pressure sensor is desired to obtain the more accurate pressure data.

In conclusion, there are some limitations in our experiment setup and method, which need to be optimized in the future work to improve the accuracy of results. Nevertheless, the piezoelectric pressure sensor exhibit high sensitivity and good linearity to the pulse pressure, which meets the requirement of our research objective.

5.0 AIR BLAST PRESSURE MEASUREMENT

5.1 EXPERIMENT SETUP DESIGN

Another experiment setup was also designed to investigate the transient response of PZT thick film sensor under more intense pressure loading. An air shock tube was fabricated as shown in Figure 5-1, which consists of two sections. The driver section is the high pressure chamber supplied by the high pressure air from the air reservoir. The driven section is the low pressure chamber which is connected to the atmosphere at the open end. The two sections are coupled with bolts on the flange of each section. A membrane divides them between the flanges. Six sensor-mounts, three for PZT sensor samples and three for standard pressure sensor, are welded oppositely on the driven tube. Therefore, for each test, PZT sensor sample and standard pressure sensor can be placed on the same cross section of the tube to pick the comparable pressure value. These samples and standard sensor are connected to the oscilloscope to output the data.

Due to the blast test conditions (intense and transient pressure loading) and the limitation of experiment supplies, only unimorph structures (discussed in 3.2.1) of the PZT pressure samples were tested. The samples were fabricated using tape-casting, which consists of the PZT thick film and metal substrate. Two models were selected for this study, as shown in Figure 5-2; the parameters are shown in Table 5-1.

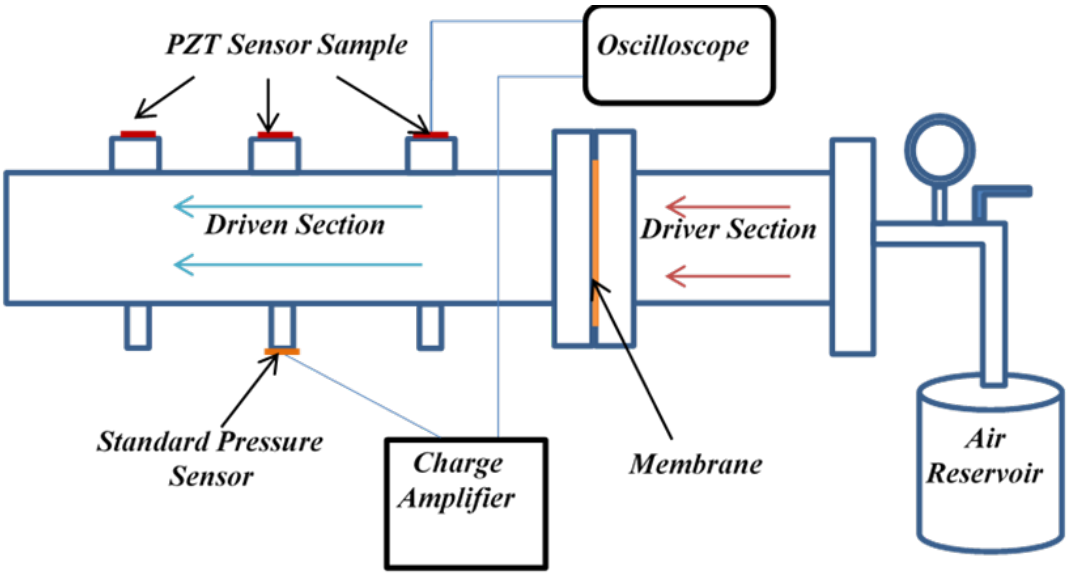

Figure 5-1. Blast pressure test setup

Figure 5-2. PZT Samples Used in Blast Pressure Test

Table 5-1 Parameters of PZT Samples (source: JCADVANCED CERAMIC LTD., CO)

Part Number	**Model A(PDH-15T60-ME)**	**Model B (PDH-12N60-NE)**
Resonant Frequency (kHz)	6.0±0.4	6.0±0.5
Resonant Impedance (ohm)	400 Max	700 Max
Capacitance (pf)	17000±30%	13000±30%
Operating Temperature (°C)	-20~+70	-20~+70
Metal Plate Diameter D (mm)	15.0±0.1	12.0±0.1
Ceramic Disc Diameter d (mm)	11.0±0.1	9.0±0.1
Metal Plate Thickness t (mm)	0.10±0.005	0.05±0.005
Total Thickness T (mm)	0.21±0.02	0.12±0.02
Metal Material	Brass	Iron Nickel Alloy

Operation steps for this setup are as follows:

1. Install PZT pressure sensor samples and standard sensor on each hole of the shock tube. Note the sensor samples on the left and right positions can record the time duration of shock wave propagation, which will be used to calculate the theoretical value of blast pressure. The sample that will be calibrated and standard sensor will be installed on the middle holes.

2. Place the membrane between the driver and driven sections, and fix these two parts with bolt connection. In order to calibrate the sensitivity and measurement range of the PZT composite samples as accurate as possible, different blast pressure should be obtained. Thus various membranes with different materials and layer are used, including latex film, aluminum foils and brass foils.

3. Release the valve of air reservoir, starting filling the driver chamber with high pressure air.

4. As the increasing of driver air pressure, the membrane will finally get ruptured, creating a blast pressure wave which propagates along in the driven tube. The pressure applied on the PZT sensor samples and standard sensor will generate electrical signals on both sensors. Therefore the blast wave form, including peak value, response time and duration, can be obtained.

5. By changing membrane materials and number of layer, different pressure waves can be generated. By comparing the data between standard sensor and our samples, we can calibrate these PZT pressure sensors.

6. Change the sensor positions to calibrate another sample.

5.2 SENSOR SAMPLES AND SETUP PREPARATION

Three PZT thickness film samples were chosen in this study, sensor 1 and 3 were made of Model A, and sensor 2 was made of Model B. A type of sensor housing was designed and fabricated using 3D printing, as shown in Figure 5.3. The PZT thick film composite discs were boundary-clamped using epoxy onto the bottom of the housing, with the metal side downward. It can be seen the mechanical model of this structure is similar with the sensor for pulse fluid pressure in chapter 4, and agrees with the conditions in theoretical analysis.

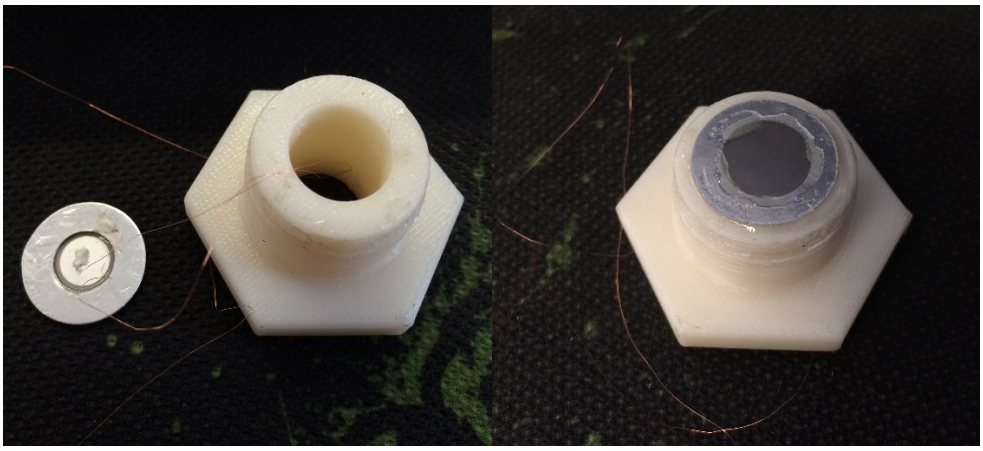

Figure 5-3. Sensor Housing

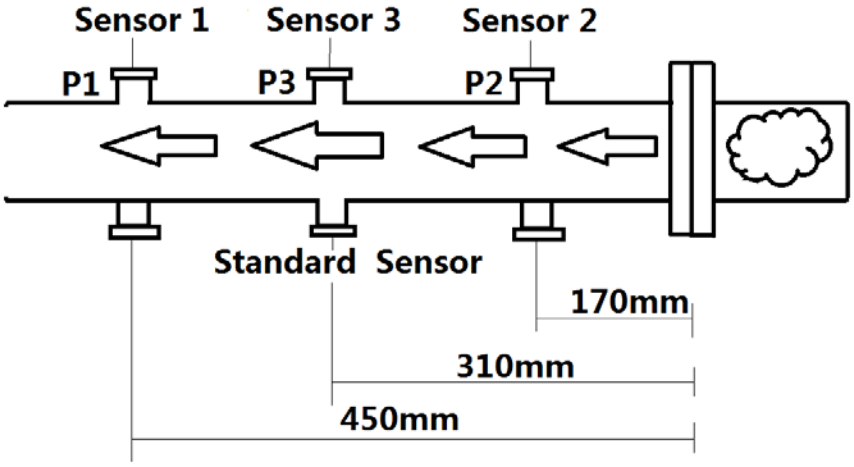

Figure 5-4. Sensor Installation Positions

A shock tube was fabricated with 800mm length, 61mm out diameter and 52inner diameter. Six holes were machined oppositely on three positions of the tube, and pipe coupling was wielded on each hole. As shown in Figure 5.4, Sensor 1, 2, 3 were installed on position 1, 2, 3, respectively, and a standard pressure sensor (PCB piezotronics^{INC}, 116B02) was installed on position 2 to get the reference air blast pressure value. Three kinds of membranes were used in

this experiment, which were shown in Table 5-2. Figure 5.4 shows the complete setup of this experiment.

Table 5-2 Membrane Parameters

Material	Thickness(in)	Number of Layer
Latex	0.006	1, 2
Aluminum	0.001	1
Mylar	0.0005	1

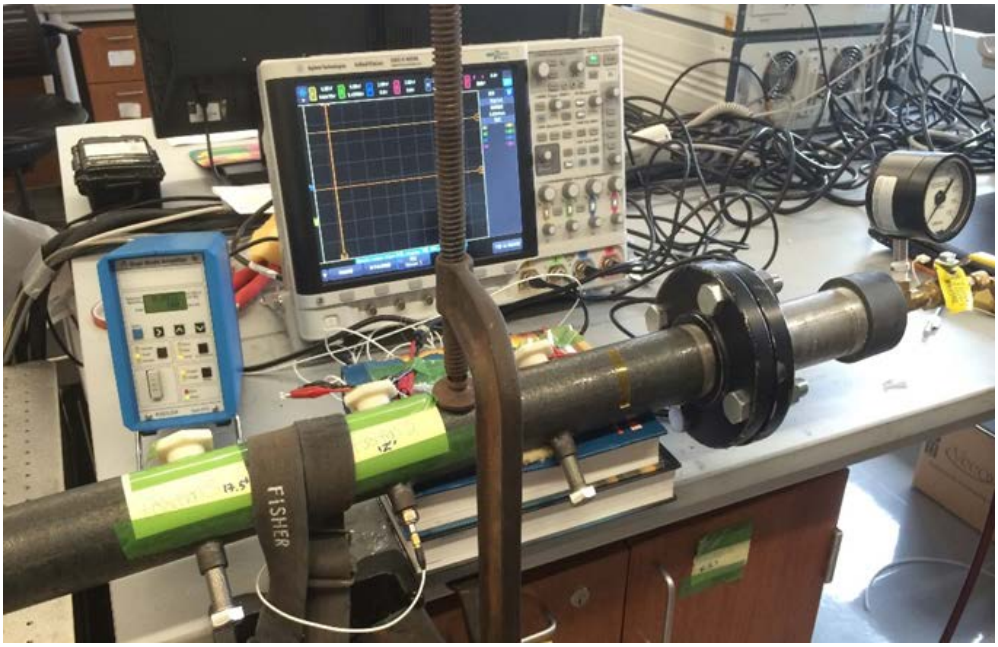

Figure 5-5. Air Blast Pressure Test Setup

5.3 EXPERIMENT RESULTS

5.3.1 Blast Pressure Waveforms

14 tests were recorded as the valid data for each sensor. Due to the difference of various kinds of membranes, the blast pressure range was about 0 to 55kPa. It is desirable to test each sensor sample on the middle position of the tube to get the most accurate result. Due to the limitation of membrane materials, however, only sensor 3 was calibrated on the same position (P2) of standard sensor. Although the other two samples were calibrated on their origin positions (P1 and P3), the error from the pressure difference should be acceptable for the relatively short distance between each position.

Partial test results were shown in Figure5.6:

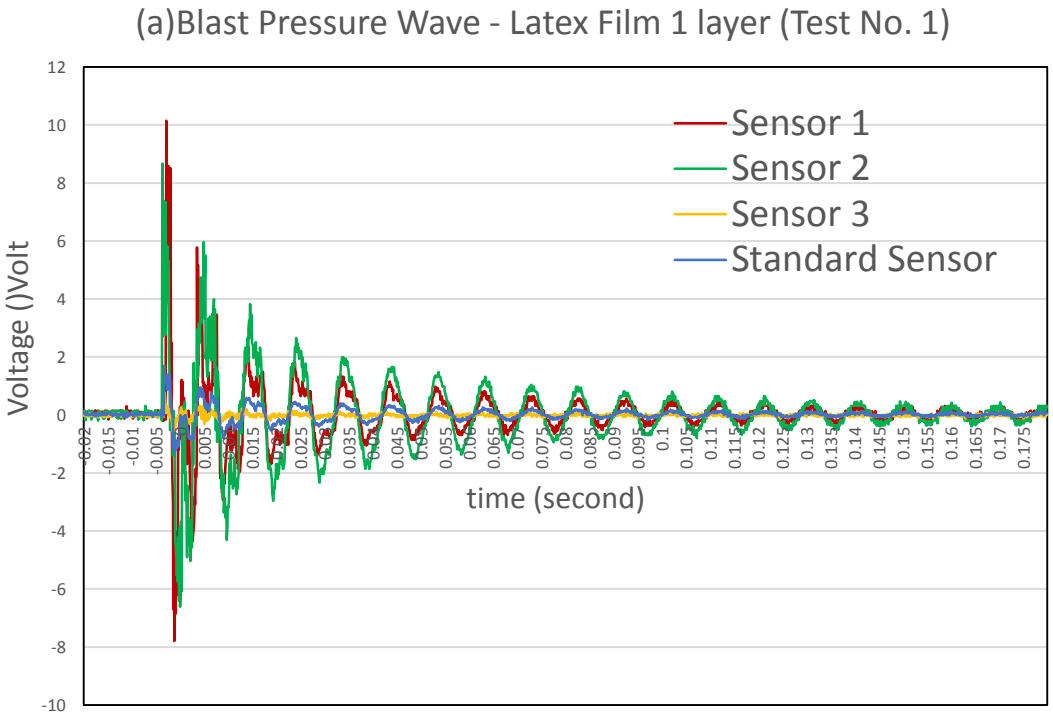

(b) Blast Pressure Wave - Aluminum Foil 1 layer (Test No.6)

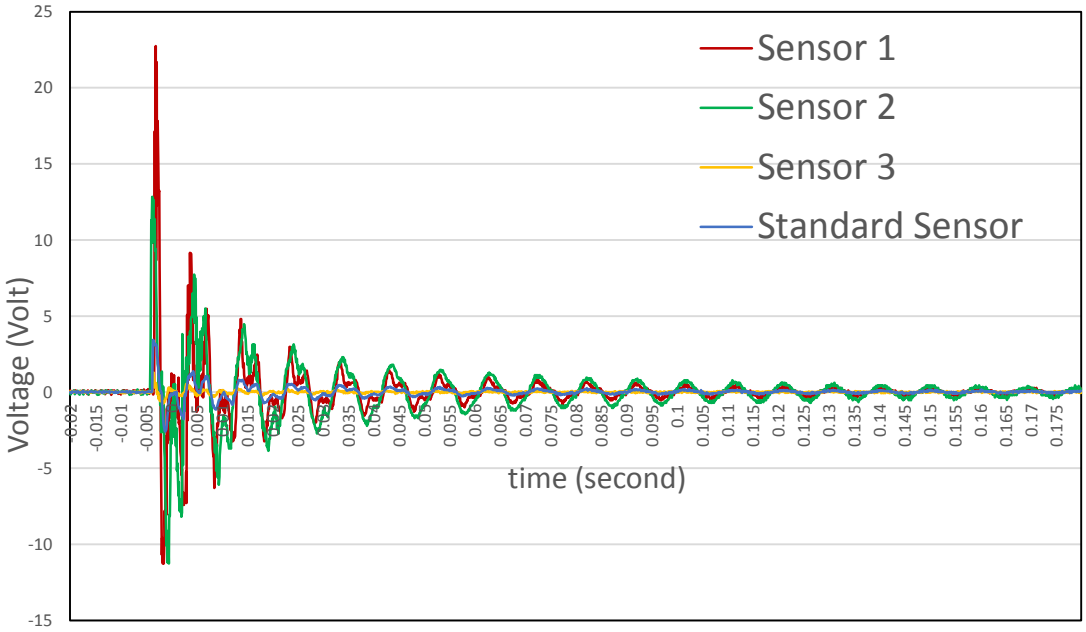

(c) Blast Pressure Wave - Aluminum Foil 1 layer (Test No.7)

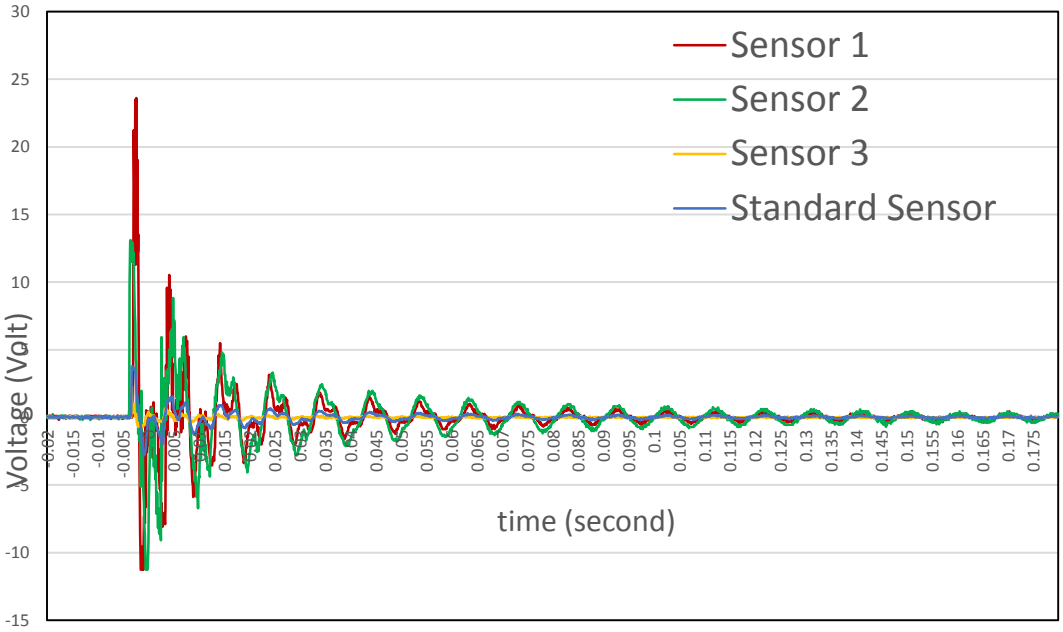

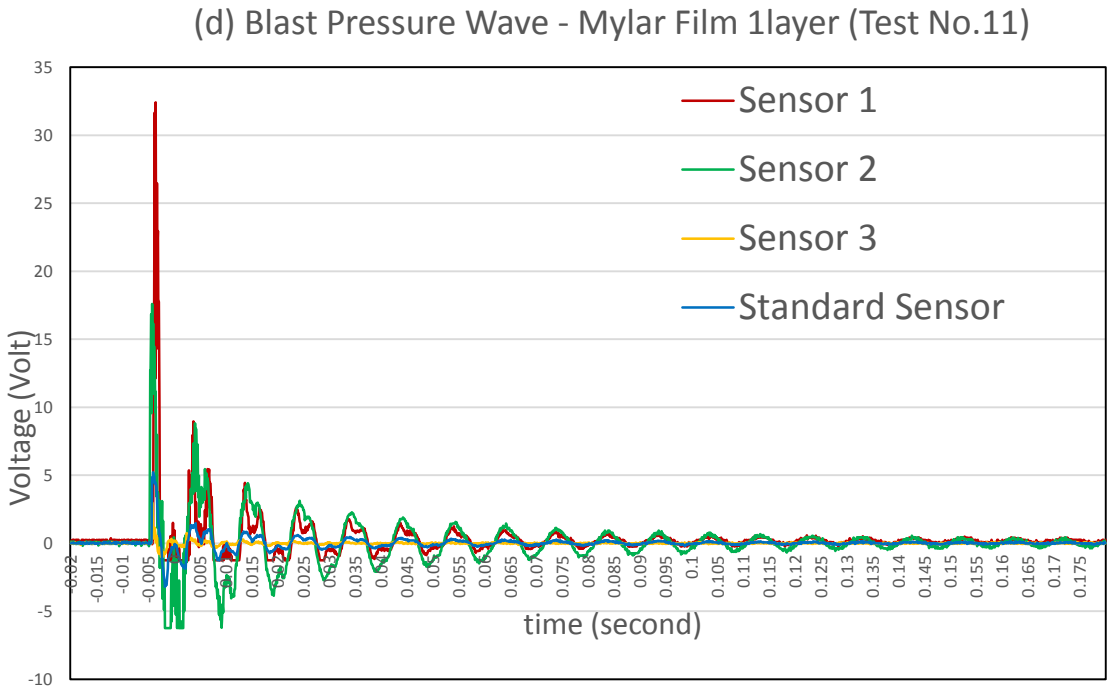

Figure 5-6. (a)-(b) Partial Test Results of Blast Pressure Wave

Other tested pressure waveforms are omitted here. By comparing the peak values of each sensor output with the standard pressure sensor signal, the calibration curves can be obtained. The peak pressure data of all 14 tests were recorded in Table 5-3.

Table 5-3 Peak Pressure Data

Test No.	***Membrane/layer***	***Sensor 1 (V)***	***Sensor2 (V)***	***Sensor3 (V)***	***Std Sensor (V)***	***Reference Pressure (kPa)***
1	*Latex, 1*	*11.7*	*8.7*	*1.0*	*2.0*	*20*
2	*Latex, 1*	*9.7*	*8.2*	*0.66*	*1.6*	*16*
3	*Latex, 1*	*10.5*	*8.0*	*0.87*	*1.81*	*18.1*
4	*Latex, 1*	*12.2*	*9.5*	*1.0*	*2.01*	*20.1*
5	*Al foil, 1*	*18.5*	*11.3*	*1.2*	*2.87*	*28.7*
6	*Al foil, 1*	*25.1*	*13.0*	*1.67*	*3.67*	*36.7*

Table 5-3 (Continued)

Test No.	*Membrane/layer*	*Sensor 1 (V)*	*Sensor2 (V)*	*Sensor3 (V)*	*Std Sensor (V)*	*Reference Pressure (kPa)*
7	*Al foil, 1*	*22.2*	*11.8*	*1.34*	*3.28*	*32.8*
8	*Al foil, 1*	*31.3*	*14.7*	*2.34*	*4.15*	*41.5*
9	*Al foil, 1*	*30.3*	*14.2*	*2.21*	*3.95*	*39.5*
10	*Al foil, 1*	*22.2*	*12.6*	*1.34*	*3.35*	*33.5*
11	*Al foil, 1*	*29.2*	*14.7*	*2.14*	*3.88*	*38.8*
12	*Mylar, 1*	*37.5*	*20*	*3.35*	*5.15*	*51.5*
13	*Mylar, 1*	*38.6*	*20.4*	*3.55*	*5.42*	*54.2*
14	*Mylar, 1*	*33*	*18.6*	*2.74*	*4.55*	*45.5*

5.3.2 Theoretical Calculation of Shock Tube Pressure

A theoretical method to obtain the shock tube pressure magnitude was introduced in this study [cite here]. First step is measuring the time interval Δt of the pressure wave propagation between position 1 and 2 according to the oscilloscope cursor, then calculating the average wave speed v in the tube:

$$v = \frac{\Delta x}{\Delta t} \qquad (5.1)$$

where Δx is the distance between position 1 and 2, which is about 280mm in this study. Δt can be measured through the wave form data, as shown in Figure 5.7 for example. Table 5-4 records the Δt of all 14 tests.

Table 5-4 Time Interval of Each Test

Test No.	1	2	3	4	5	6	7	8	9	10	11	12	13	14
Δt(μs)	750	760	756	750	726	708	712	702	704	710	706	680	676	694

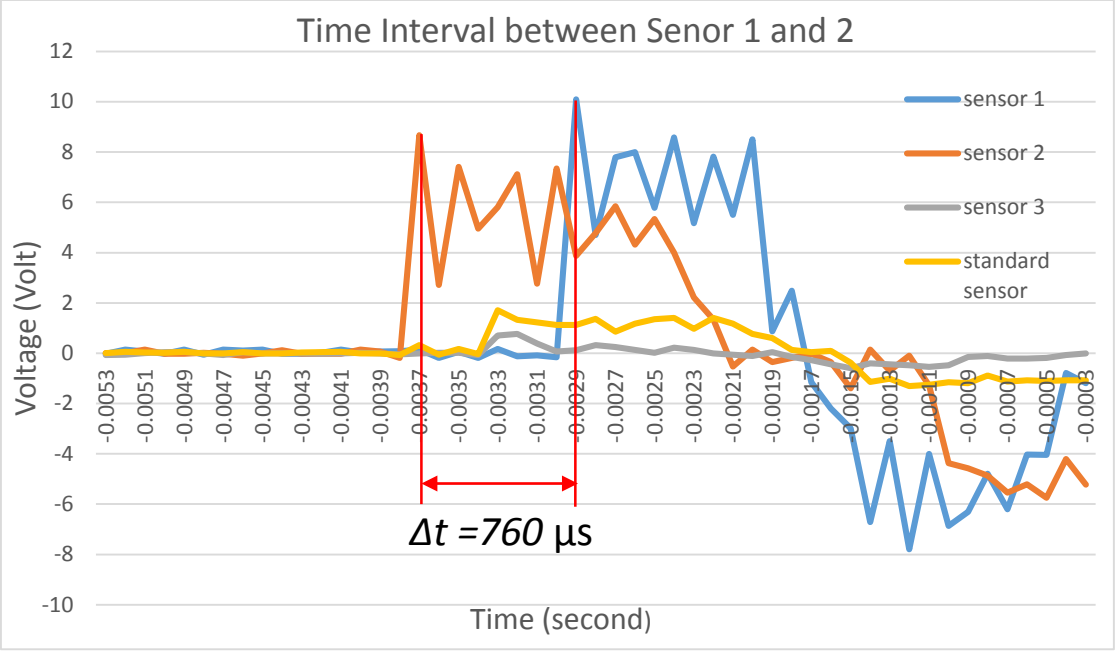

Figure 5-7. Time Interval Measurement

The overpressure Δp thus can be calculated by shock wave equation:

$$\frac{\Delta p}{P_0} = \frac{P - P_0}{P_0} = \frac{2k}{k+1}(M^2 - 1) \qquad (5.2)$$

Where P is the absolute shock pressure, P_0 is standard atmosphere pressure, P_0 = 101.325kPa. k is a constant that which is 1.4 for air. M is the Mach number of shock wave, $M=v/C_0$. C_0 is the initial velocity of sound in driven chamber, which is related to ambient temperature T. $C_0=331.6+0.54T$. In this study, $T=25°C$. Substituting Δt into above equations, the theoretical peak pressure values can be obtained, as shown in Table 5-5:

Table 5-5 Theoretical Peak Pressure of each Test

Test No.	1	2	3	4	5	6	7	8	9	10	11	12	13	14
Value(kPa)	20.1	16.5	17.9	20.1	29.4	37	35.3	39.7	38.8	36.2	37.9	50.1	52.1	43.4

5.3.3 Calibration Curves of Sensor Samples

The calibration curves of each sensor sample can be drawn by the relationship between generated peak voltage magnitudes vs. reference pressure and theoretical values, as shown in Figure 5.8:

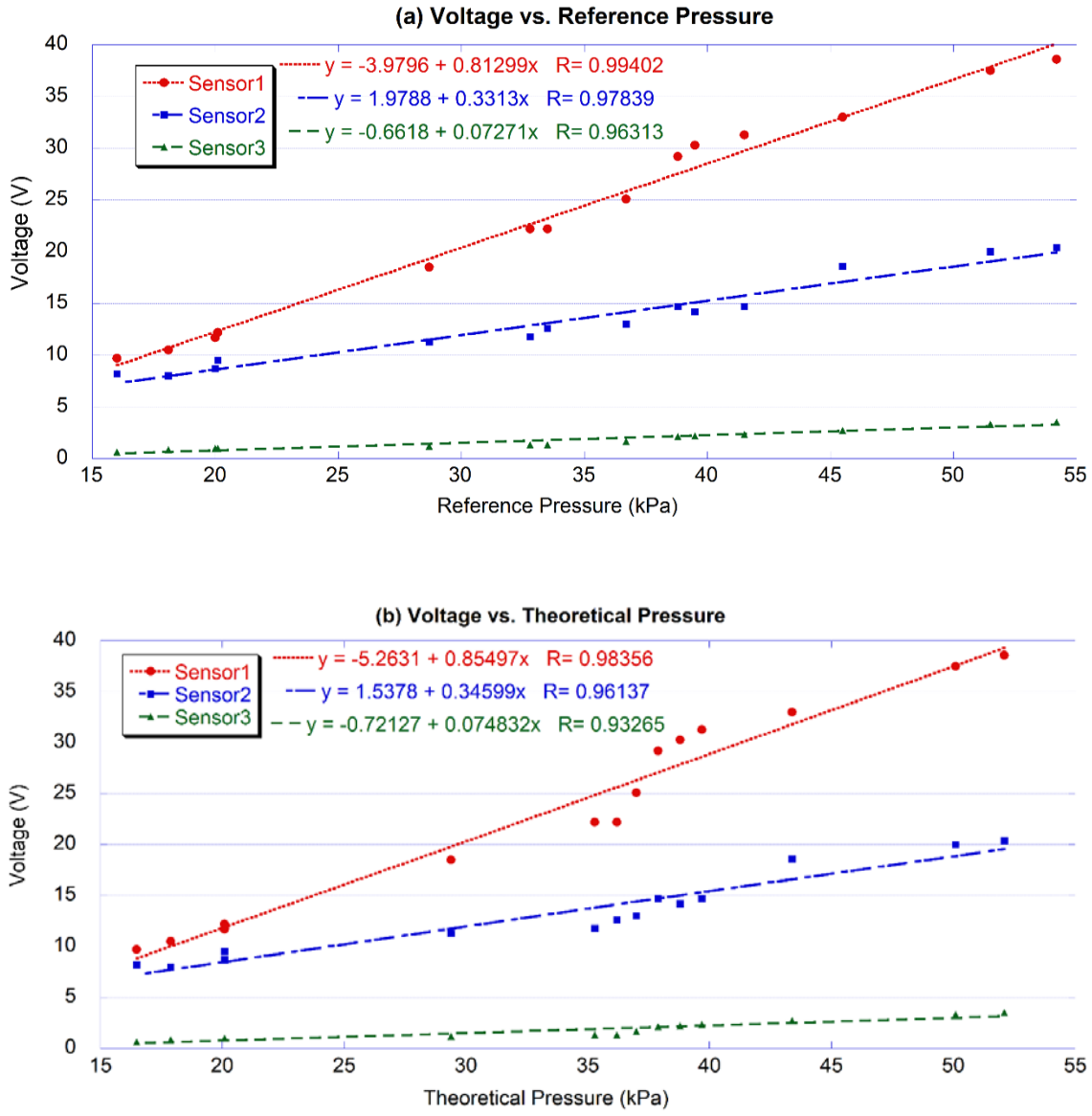

Figure 5-8. Calibration Curves of Each Sensor Sample: (a) Calibrated by Reference Pressure (standard sensor); (b) Calibrated by Calculated Pressure

5.4 ANALYSIS AND DISCUSSION

It is clear that the calibrations in Figure 5.8(a) and (b) are almost linear in the measured range for the three sensor samples. Compared the sensitivities obtained by two methods, the one that uses a standard sensor to indicate the reference pressure is slight lower than the corresponding one calibrated by ideal shock wave equations. The errors may exist in both methods. For the standard sensor, the manufacturer's calibration may get inaccurate due to use and aging; for the theoretical calculation, the deviation mainly comes from the observation error of the arrival times at two different sensor positions. Although it is unclear which method is more accurate, the result differences are very slight. For simplicity, only the results from the first method will be discussed.

The scattered points were fitted by least square approximation to get the relations between voltage (V) and pressure (kPa), which are: $V_1=-0.398+0.813\ P_1$, $V_2=1.538+0.346P_2$ *and* $V_3=-0.662+0.073P_3$, for sensor 1 2, and 3, respectively. Thus the sensitivity for each sample is s_1=813mV/kPa, s_2=346mV/kPa, and s_3=73mV/kPa. The standard sensor (PCB116B02), of which the capacitance is 25.7pf, has a voltage sensitivity s_p= 36.2mV/kPa. Therefore, the three PZT thick film sensor samples have much larger sensitivities than the standard sensor.

The theoretical sensitivity of these three sensor models are also calculated by Equation 3.29, Figure 5-9 shows the simulation curves of each sensors, and Table 5-6 shows the comparison between experimental and theoretical values.

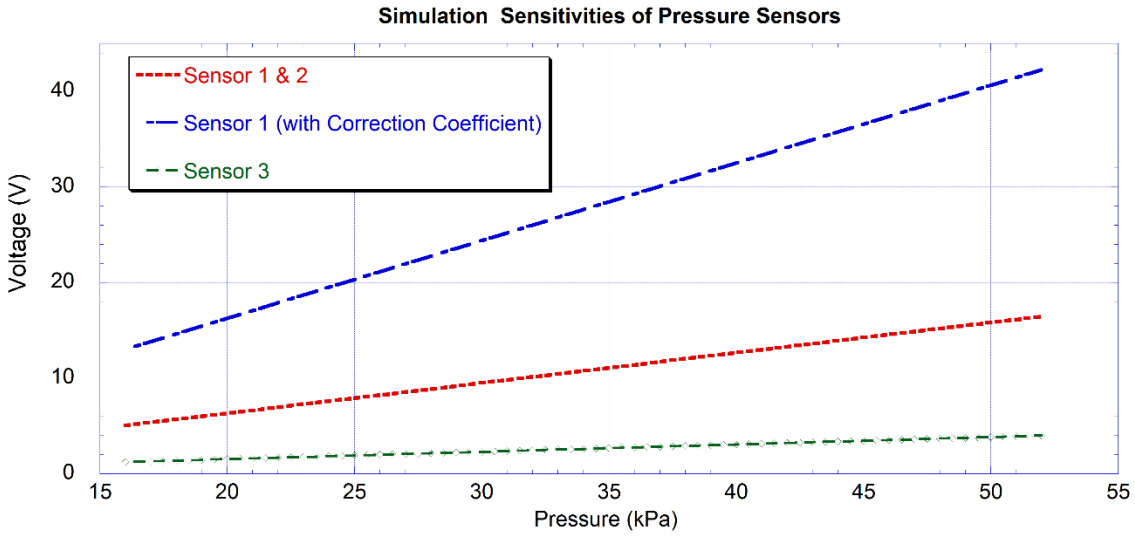

Figure 5-9. Simulation Results of Sensitivity (Sensor 1 with Correction Factor=2.5)

Table 5-6 Comparison of Experiment and Theoretical Sensitivities

Sensor Model	Sensitivity (mV/kPa)		
	Experimental		Theoretical
	Method 1	Method 2	
Sample 1	813	854	316.7
Sample 2	331	346	316.7
Sample 3	72.7	74.8	77.08
Standard	36.2	N/A	N/A

According to Figure 5-9 and Table 5-6, the experimental values of sensor sample 2 and 3 agree well with the theoretical sensitivities, which is 345.56 and 74.75 mV/kPa, respectively.

The sensitivity of Sensor 1 is much higher than the theoretical value, and 2.35 times more than Sensor 2 despite the sensing element of both are identical PZT sample model (Model A).

One of the most possible factor that can significantly influence the sensitivity performance is the edge condition. Compared Sample 1 with Sample 2 and 3, it is noted that the first sample uses more epoxy for bonding onto the sensor housing, of which the actual edge condition may be considered as elastically supported due to the effect of epoxy [22].The actual charge and voltage generating performance of elastically supported edge condition is between simple support and clamped support, and determined by the torsional stiffness K_t. Since the stiffness of epoxy is much lower than substrate material (E_{epoxy}=3.5 GPa), excessively use will greatly reduce K_t, resulting in higher voltage generation. Therefore a correction coefficient 2.5 is applied in the theoretical result of Sensor 1 to compensate this effect. This effect is desirable for increasing sensitivity of the sensor, however a perfect simply supported edge condition or a suitable elastically supported edge condition is difficult to make and control practically. More investigation about this issue, as well as the voltage-pressure equation under simple supported condition and the effect of torsional stiffness K_t should be done in future work. Compared the unimorph structure with sandwiched structure, it is assumed that the former one has larger electromechanical coupling effect due to simpler structure and less layers, which results in higher energy convert efficiency. The sandwiched structure, however, is more flexible due to the cover layers of PZT film and pre-thermal stress in the film. It can be conclude that unimorph structure sensor is more suitable for relatively transient and intensive pressure loading, such as blast pressure; whereas sandwiched structure sensor is favorable for low frequency, continuous pressure loading, such as human pulse pressure and ocean wave pressure.

6.0 SENSOR RESPONSE TO HUMAN PULSE PRESSURE

6.1 INTRODUCTION

In this section, the effectiveness of sandwiched PZT pressure sensor samples in human arterial pulse wave detection was studied. The propagation of human arterial pulse wave is an important sign to indicate arterial stiffness, physiological changes in peripheral vascular disease and other health conditions. Various methods and sensors, such as optical sensors, laser Doppler sensors and piezoelectric sensors have been used to detect pulse waves at different artery regions. For piezoelectric-based sensors, the mechanical energy from arterial pulse pressure can be converted to charge signal directly, with relatively high sensitivity, improved hysteresis, excellent repeatability, and high durability [29]. Since the human skin has various surface topologies, it requires the sensor to be flexible. Investigations on flexible piezo-pulse pressure sensors include AlN [15], PZT thin film [29], PVDF [31, 32], etc. Most of these sensors are thin film structures, which are up to few microns in thickness due to difficulty of materials' fabrication, therefore the generated charge signals are relatively weak comparing with the PZT thick film in our study. The experiment result for our samples showed a good compatibility on human skin surface and high sensitivity of weak arterial pressure.

6.2 EXPERIMENT

6.2.1 Experimental principle and setup

The arterial pulse wave velocity (PWV) is defined as the distance traveled by the wave divided by the time to travel that distance. There are various arterial regions of human body, as shown in Figure 6.1(left). Pulse amplitude s and PWV between different arterial regions are varied. In our study, the pulse wave at brachial (mid arm) artery and radial (wrist) artery of one person were measured, and the PWV between them was estimated. Two PZT thick film sensors were bonded on these two regions and detected the pulse pressure changes simultaneously. The generated electric signals were amplified by charge amplifier and the wave forms were read out by a two-channel oscilloscope, as shown in Figure 6.1(right). The PWV thus can be estimated by the distance *D* between two regions divided by the time difference between two successive peaks of two waveforms

$$PWV = D / \Delta t \qquad (6.1)$$

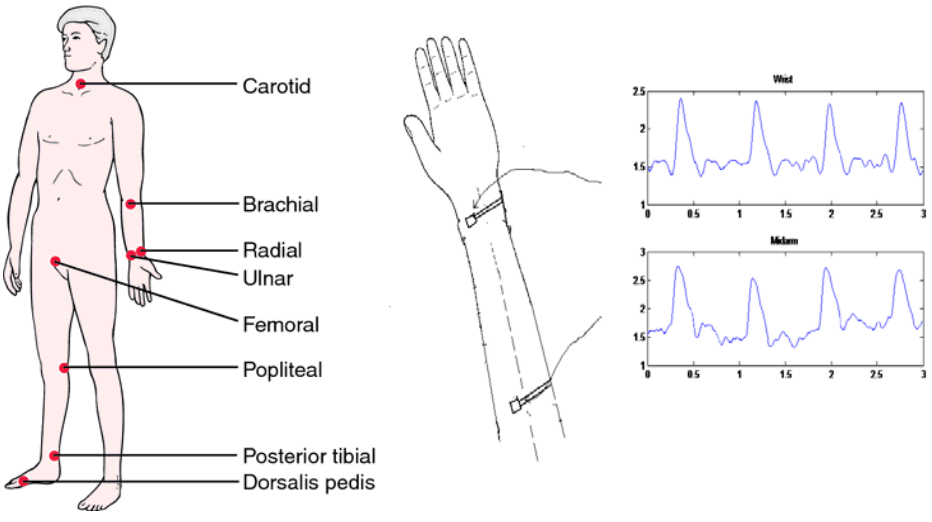

Figure 6-1.Pulse Wave Velocity measurements: Left: Arterial regions in human body [31].Right: measure PWV between brachial and radical arteries [32].

6.2.2 Result and Discussion

Firstly, the pulse wave forms of radial and brachial regions were detected respectively, which were shown in Figure 6-2. Both two waveforms have the same pulse frequency as about 1.1 Hz, which matches the heart rate (65-70 bpm) of the tested person. The amplitude of radial pulse wave is larger than the brachial one. It is because that the distance between the surface of skin at wrist is shorter than that at mid arm region. Nevertheless, the PZT pressure sensor successfully detected these pulse pressures when bonded on the skin surfaces, demonstrating its high flexibility and sensitivity.

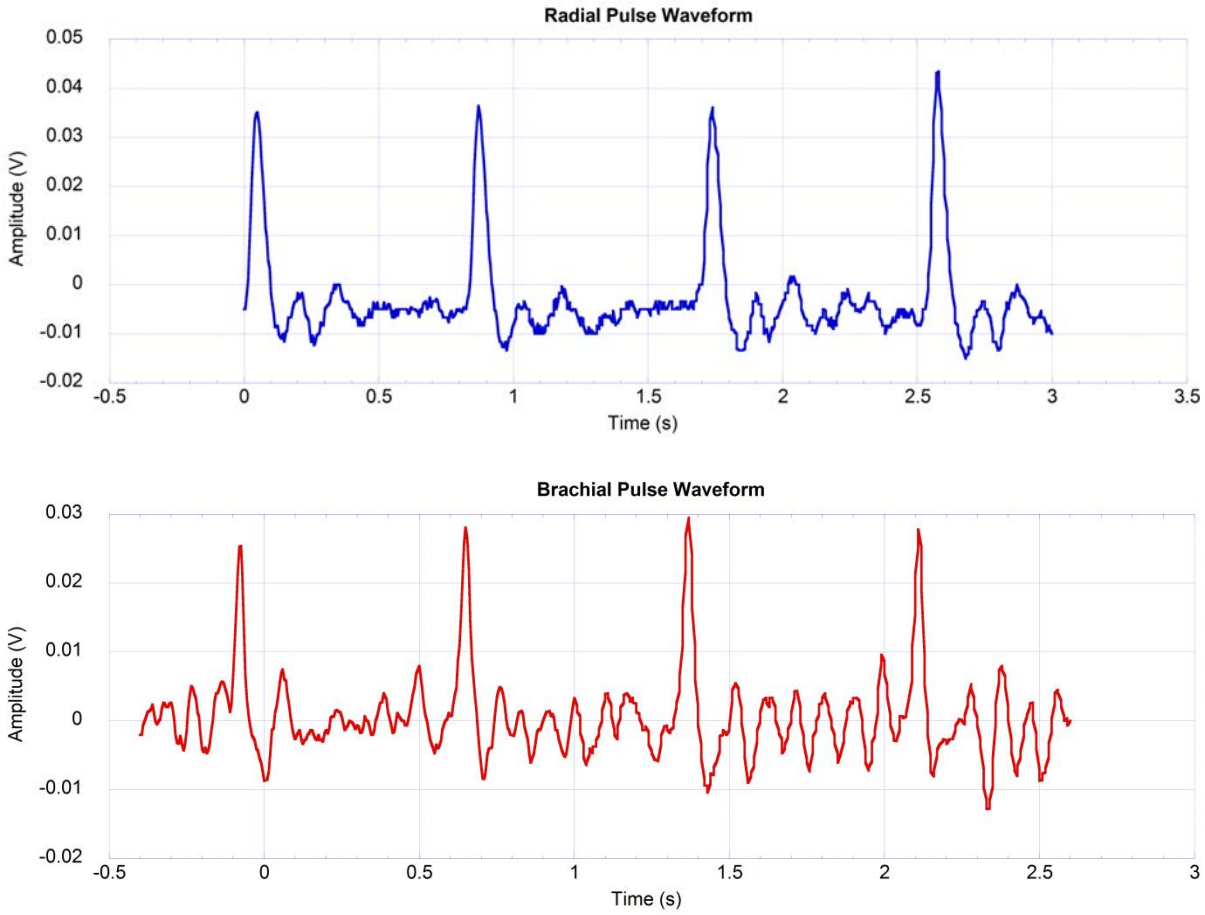

Figure 6-2. Pulse waveforms detected by PZT sensors: Upper: Radial. Lower: Brachial

Then, in order to estimate the pulse wave velocity (PWV), these two pulse signals were measured simultaneously, shown in Figure 6-3. The time interval between brachial to radial arteries is about 65±5ms, and for the tested person the distance between two positions is about 0.25m. Thus the estimated value of Brachial- Radial PWV by equation (6.1) is about 3.6-4.2m/s, which is consistence with a recent publication using PZT thin film sensors which reports the result of 4m/s [32].

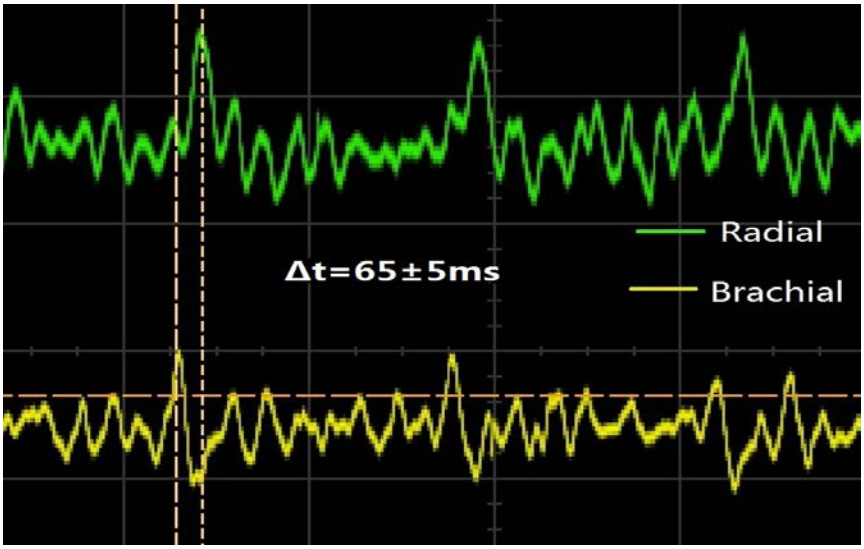

Figure 6-3. The time interval between the brachial to radial

6.3 CONCLUSION

The PZT thick film pressure sensors can be used in human pulse wave measurement, including pulse rate detection and pulse wave velocity estimate. The PZT pressure sensor is flexible enough to be bonded onto the various skin surfaces such as mid arm region and wrist region. It is sensitive to low frequent radical and brachial arterial pulses, and the estimated PWV value

obtained by the sensor was reliable. Due to its high flexibility, high sensitivity and non-invasive sensing method, this PZT thick film pressure senor is useful in human health monitoring.

7.0 CONCLUSION AND FUTURE WORK

The main objective of this thesis is to investigate the feasibility of the PZT piezoelectric thick film as the circular diaphragm sensor for different kinds of pressure measurement, including low frequency periodical pressure loading and transient blast pressure loading.

Using tape-casting method, the thickness of PZT ceramic films can be controlled in the range from tens to hundreds of micrometers, which are defined as PZT thick films. The advantage of PZT thick film as pressure sensor lies on both its mechanical flexibility and piezoelectric property. Compared with bulk PZT, thick film structure is much more flexible and deformable, which is desired for many pressure sensing environments such as human skin surface and pipeline wall. Meanwhile, the highest piezoelectric constant and electric-mechanical coupling coefficients of this material make it stand out from other flexible pressure sensing material such as AlN, ZnO and PVDF. Therefore, PZT thick film is very promising to be applied into diaphragm pressure sensor.

The sensor structure was designed as circular composite which consist of piezoelectric layer and flexible metal substrate. The relationship between sensor output charge and voltage as results of applied pressure was derived theoretically, as well as the dynamic frequency effect. It can be shown that the output electric signals are proportional to the pressure change, which can be used to calibrate the sensitivity of pressure senor.

Sandwiched and unimorph sensor structure were compared, the first one was chosen for the pulse pressure measurement due to its better robustness and flexibility, whereas the latter one for blast pressure testing due to higher structural stiffness and electromechanical coupling effect. The fabrication process of each sensor structure was introduced step by step. Specific calibration setups were designed and fabricated to test the performance of these two kinds of sensor samples. For fluid pulse pressure testing, the setup includes a peristaltic pump, a flow chamber and a water tank, which act as a circulating pulsate water loop. The sensor sample was fixed onto the chamber surface to detect different pulse pressures caused by pump motion. A ‘disk deflection’ method was used to calibrate the amplitude of pressure variation. For blast pressure testing, the setup main consists of a shock tube and oscilloscope. Samples with different thickness and radii were fixed on different positions of the tube, and a standard sensor was used for reference.

The experiment results of fluid pulse pressure experiment showed that the output voltage of piezoelectric sensor is proportional to the pressure change at certain pulse frequency, which agrees with the analytical analysis and theoretical results. The calibration curve between voltage and pressure can be obtained from experimental data, which enables to monitor pressure change quantitatively. However, the sensitivities of each sample slightly vary under different pulse frequencies, which may result from the inaccuracy of pressure calibrate method, as well as the disturbance of noise flow and ambient vibration. Therefore, the test setup needs to be improved on the following aspects. First of the all, the ‘disk deflection’ method used to calibrate the pressure amplitude should be modified. Given that the actual experiment conditions may not satisfy the assumption of small bending theory, the deflection change of the metal disk may not reflect the pressure variation accurately and promptly, thus resulting measurement errors. And

the optic vibrometer may contribute additional errors due to its sensitivity to ambient vibrations. In order to improve the accuracy of pressure calibration, a standard commercial pressure sensor should be applied. And the position of this sensor also needs to be optimized. The second limitation is the design of chamber shape. Since the width of chamber is larger than the inlet and outlet tube, turbulence flows may generate in the chamber, which increases the uncontrollability of applied pressure. In the future research, it is recommended to redesign the chamber with the help of CFD software such as ANSYS Fluent to get the optimum shape. The third limitation is that the pressure sensor samples in our study are restricted by the PZT thick films' quality and quantity. Due to the limited number and types of PZT films, only several samples with one thickness (70 microns) were fabricated and tested. In the future research, more samples with different radii and thicknesses should be investigated and compared. More theoretical work should be conducted to find the optimum dimensions and volume ratios of the sensor structure.

In the experiment of blast wave pressure sensor, each sample with different size showed almost linear relationship to pressure change in the range up to 55kPa. During the experiment, it was found that one of the sensor sample generated much higher voltage than theoretical simulation result. This can be explained by the elastically supported edge issue which may cause by overused epoxy, which is desirable for sensitivity improvement but unfavorable for practical fabrication. More investigation about this issue, as well as the voltage-pressure equation under simple supported condition and the effect of torsional stiffness K_t should be done in future work. Nevertheless, voltage sensitivity of each sensor is higher than the standard pressure sensor. The practical application of this kind of sensor will be further investigated in the future work, such as the blast-induced mild traumatic brain injury (bTBI) in military conflicts [34].

The feasibility of sandwiched pressure sensor sample used in practical human blood pulse detection was also studied. Distinguishable pulse wave signals can be obtained on both the brachial and radical regions of human body. And the pulse wave velocity between these two positions can be calculated from the time difference of waveforms detected by our sensors.

APPENDIX A

THEORETICAL DERIVATION PROCESS USING MATHEMATICA 10.0

1. Expressions of W functions and Constants C1-C8

DSolve[1/r*(∂/∂r)(r*(∂/∂r)(1/r*(∂/∂r)(r*∂w(r)/∂r)))==p/d,w(r),r]

wo[r]=(p r^4)/(64 d)+1/2 r^2 C[2]-1/4 r^2 C[3]+C[4]+C[1] Log[r]+1/2 r2 C[3] Log[r]

wi[r]=(p r^4)/(64 d)+(r^2 C6)/2+C8

Solve[{(p a^4)/(64 do)+1/2 a^2 C[2]+C[4]+C[1] Log[a]==0,(p a^3)/(16 do)+C[1]/a+a C[2]==0,(p b^4)/(64*do)+1/2 b^2 C[2]+C[4]+C[1] Log[b]==(p b^4)/(64 di)+(b^2 C[6])/2+C[8],(p b^3)/(16 do)+C[1]/b+b C[2]==(p b^3)/(16 di)+b C[6],-((p b^4 (3+v0)+16 d0((-1+v0) C[1]+b^2 (1+v0) C[2]))/(16 b^2))==-C[6] di(1+vi)-1/16 p r^2 (3+vi)},{C[1],C[2],C[4],C[6],C[8]}]

C1=(a^2 b^2 p (a^2 (d0-di) (1+v)+do r^2 (3+v)+b^2 (di (1+v)-2 do (2+v))))/(16 do (-b^2 (d0-di) (1+v)+a^2 (d0 (-1+v)-di (1+v))))

C2=(p (a^4 (d0+di-d0 v+di v)-b^2 (do r^2 (3+v)+b^2 (di (1+v)-2 do (2+v)))))/(16 do (-b^2 (d0-di) (1+v)+a^2 (d0 (-1+v)-di (1+v))))

C4=(a^2 p (a^2 b^2 (d0-di) (1+v)+a^4 (d0 (-1+v)-di (1+v))+2 b^2 (do r^2 (3+v)+b^2 (di (1+v)-2 do (2+v)))-4 b^2 (a^2 (d0-di) (1+v)+do r^2 (3+v)+b^2 (di (1+v)-2 do (2+v))) Log[a]))/(64 do (-b^2 (d0-di) (1+v)+a^2 (d0 (-1+v)-di (1+v))));

C6=(p (-2 a^4 d0 di+b^2 (di do r^2 (3+v)+b^2 (d0 (di-do) (1+v)-di do (3+v)))+a^2 (-di do r^2 (3+v)+b^2 (-d0 (di-do) (-1+v)+di do (3+v)))))/(16 di do (b^2 (d0-di) (1+v)+a^2 (d0+di-d0 v+di v)))

C8=(p ((a^4 di+b^4 (-di+do)) (b^2 (d0-di) (1+v)+a^2 (d0+di-d0 v+di v))+4 a^2 b^2 di (a^2 (d0-di) (1+v)+do r^2 (3+v)+b^2 (di (1+v)-2 do (2+v))) Log[a]-4 a^2 b^2 di (a^2 (d0-di) (1+v)+do r^2 (3+v)+b^2 (di (1+v)-2 do (2+v))) Log[b]))/(64 di do (b^2 (d0-di) (1+v)+a^2 (d0+di-d0 v+di v)))

wo=p*r^4/(64*do)+1/2*C2*r^2+C1*Log[r]+C4

wi=p*r^4/(64*di)+1/2*C6*r^2+C8

2. Derive Moment M functions from W function

M_{rc}=-di*(D[wi, {r, 2}] + v/r*D[wi, r])

M_{rm}=−do∗(D[wo,{r,2}]+vr∗D[wo,r])

$M_{\theta c}$=-di(-1/r∗D[wi,r]+v∗D[wi,{r,2}])

$M_{\theta m}$=-do(1/r*D[wo, r] + v*D[wo, {r, 2}])

M_{rc}=1/(16 do (-b^2 (d0-di) (1+v)+a^2 (d0 (-1+v)-di (1+v)))) p (-2 a^4 d0 di (1+v)+b^2 (do r^2 (3+v) (d0+5 di+(d0+di) v)+b^2 (1+v) (d0 (di-do) (1+v)-di do (3+v)))+a^2 (-b^2 (1+v) (d0 (di-do) (-1+v)-di do (3+v))-do r^2 (3+v) (d0 (-1+v)+di (5+v)))+2 a^2 b^2 di do (1+v) (3+v) (Log[a]-Log[b]))

M_{rm}=1/(16 r^2 (-b^2 (d0-di) (1+v)+a^2 (d0 (-1+v)-di (1+v)))) p (-a^4 (1+v) (b^2 (d0-di) (-1+v)+r^2 (d0+di-d0 v+di v))+a^2 (-2 b^2 do r^2 (2+v) (3+v)-r^4 (3+v) (d0 (-1+v)-di (1+v))-b^4 (-1+v) (di (1+v)-2 do (2+v)))+b^2 r^2 (b^2 (1+v) (di (1+v)-2 do (2+v))+r^2 (3+v) (d0 (1+v)-di (1+v)+2 do (3+v)))+2 a^2 b^2 do r^2 (1+v) (3+v) (Log[a]-Log[r]))

$M_{\theta c}$=1/(16 do (-b^2 (d0-di) (1+v)+a^2 (d0 (-1+v)-di (1+v)))) p (-2 a^4 d0 di (1+v)+b^2 (do r^2 (1+3 v) (d0+5 di+(d0+di) v)+b^2 (1+v) (d0 (di-do) (1+v)-di do (3+v)))+a^2 (-b^2 (1+v) (d0 (di-do) (-1+v)-di do (3+v))-do r^2 (1+3 v) (d0 (-1+v)+di (5+v)))+2 a^2 b^2 di do (1+v) (3+v) (Log[a]-Log[b]))

$M_{\theta m}$=1/(16 r^2 (-b^2 (d0-di) (1+v)+a^2 (d0 (-1+v)-di (1+v)))) p (a^4 (b^2 (d0-di) (-1+v^2)+r^2 (1+v) (d0 (-1+v)-di (1+v)))+a^2 (-2 b^2 do r^2 (3+v) (1+2 v)+r^4 (d0+di+2 (d0+2 di) v+3 (-d0+di) v^2)+b^4 (-1+v) (di (1+v)-2 do (2+v)))+b^2 r^2 (b^2 (1+v) (di (1+v)-2 do (2+v))+r^2 (1+3 v) (d0 (1+v)-di (1+v)+2 do (3+v)))+2 a^2 b^2 do r^2 (1+v) (3+v) (Log[a]-Log[r]))

3. Derive Curvature functions k from Moment M functions

z0=(hp^2*sm*b-hm^2*s11*a)/(2*(s11*hm*a+sm*hp*b))

Integrate[-((d31 E3+krp(z-z0)+d31 E3 v+kθp(z-z0) v)/(s11 (-1+v^2)))*(z-z0),{z,0,hp}]+

Integrate[-((krp(z-z0)+kθp(z-z0)*v)/(sm(-1+v^2)))*(z-z0),{z,-hm,0}] (*Mrc*)

Integrate[-((d31E3+kθp(z-z0)+d31E3v+krp(z-z0)v)/(s11(-1+v^2)))*(z-z0),{z,0,hp}]+Integrate[-((kθp(z-z0)+krp(z-z0)*v)/(sm(-1+v^2)))*(z-z0),{z,-hm,0}](*(Mθc)*)

Integrate[-((krm(z-z0)+kθm(z-z0)*v)/(sm(-1+v^2)))*(z-z0),{z,-hm,0}](*Mrm*)

Integrate[-((kθm(z-z0)+krm(z-z0)*v)/(sm(-1+v^2)))*(z-z0),{z,-hm,0}](*Mθm*)

Mrc=-((hm (krp+kθp v) (hm^2+3 hm z0+3 $z0^2$))/(3 sm (-1+v^2)))-(hp (3 d31 E3 (1+v) (hp-2 z0)+2 (krp+kθp v) (hp^2-3 hp z0+3 $z0^2$)))/(6 s11 (-1+v^2))

Mθc=-((hm (kθp+krp v) (hm^2+3 hm z0+3 $z0^2$))/(3 sm (-1+v^2)))-(hp (3 d31 E3 (1+v) (hp-2 z0)+2 (kθp+krp v) (hp^2-3 hp z0+3 $z0^2$)))/(6 s11 (-1+v^2))

Mrm= -((hm (krm+kθm v) (hm^2+3 hm z0+3 $z0^2$))/(3 sm (-1+v^2)))

Mθm= -((hm (kθm+krm v) (hm^2+3 hm z0+3 $z0^2$))/(3 sm (-1+v^2)))

Solve[{Mrc==-((hm (krp+kθp v) (hm^2+3 hm z0+3 $z0^2$))/(3 sm (-1+v^2)))-(hp (3 d31 E3 (1+v) (hp-2 z0)+2 (krp+kθp v) (hp^2-3 hp z0+3 $z0^2$)))/(6 s11 (-1+v^2)),Mθc==-((hm (kθp+krp v) (hm^2+3 hm z0+3 $z0^2$))/(3 sm (-1+v^2)))-(hp (3 d31 E3 (1+v) (hp-2 z0)+2 (kθp+krp v) (hp^2-3 hp

z0+3 z0^2)))/(6 s11 (-1+v^2)),Mrm==-((hm (krm+kθm v) (hm^2+3 hm z0+3 z0^2))/(3 sm (-1+v^2))),Mθm==-((hm (kθm+krm v) (hm^2+3 hm z0+3 z0^2))/(3 sm (-1+v^2)))},{krp,kθp,krm,kθm}]

krp=(12 s11 sm B3^2 (Mrc-Mθc v)-6s11 sm B3 a hm d31 E3 hp (hm+hp))/B1

kθp=(12 s11 sm B3^2 (Mθc-Mrc v)-6s11 sm B3 a hm d31 E3 hp (hm+hp))/B1

krm=(12 sm B3^2 (Mrm-Mθm v))/B2

kθm=(12 sm B3^2 (Mθm-Mrm v))/B2

B1=2 a b hm hp s11 sm (hm^3 s11+hp^3 sm)+b^2 hp^2 sm^2 (4 hm^3 s11+6 hm^2 hp s11+3 hm hp^2 s11+hp^3 sm)+a^2 hm^2 s11^2 (hm^3 s11+3 hm^2 hp sm+6 hm hp^2 sm+4 hp^3 sm);

B2=hm(a^{2}hm^{4}s11^2+2 a b hm^3 hp s11 sm+b^2 hp^2(4 hm^2+6hm hp+3hp^2)sm^2);

B3=a*hm*s11+b*hp*sm;

4. Derive Expressions of Strains and Stress from Curvature functions k

z0=(hp^2*sm*b-hm^2*s11*a)/(2*(s11*hm*a+sm*hp*b));

erp=krp(z-z0);

eθp=kθp(z-z0);

erm=krm(z-z0);

eθm=kθm(z-z0);

σrpi=-((d31 E3+erp+d31 E3 v+eθp v)/(s11 (-1+v^2)))

σθpi=-((d31 E3+eθp+d31 E3 v+eri v)/(s11 (-1+v^2)))

σrmi=-((erp+eθp*v)/(sm (-1+v^2)))

σθmi=-((eθp+erp*v)/(sm(-1+v^2)))

σrmo=-((erm+eθm*v)/(sm(-1+v^2)))

σθmo=-((eθm+erm*v)/(sm(-1+v^2)))

5. Energy Density of Piezoelectric Composite Layer and Substrate

dUp=12∗erp∗σrpi+12∗eθp∗σθpi−d31^2∗(σrpi+σθpi)∗E3+12∗e33∗E3^2

dUmi=12∗erp∗σrmi+12∗eθp∗σθmi

(*long expressions are omitted here*)

6. Integrate Total Energy from Energy Density

Upz=Integrate[dUp,{z,0,hp}]

Up=Integrate[Upz∗r,{θ,0,2Pi},{r,0,b}]

Umiz=Integrate[dUmi,{z,−hm,0}]

Umi=Integrate[Umiz∗r,{θ,0,2Pi},{r,0,b}]

Utotal=Up+Umi

7. Derive Total Charge Output from Total Energy

E3=V3/hp

Qtotal=D[Upp+Umi,V3]

Qgen=Qtotal at V3=0,

Qgen=−3ab^{2}B3^{3}d31dihm(hm+hp)$p\pi$s11sm(a^2hm^{5}s11^3+$a$hm^{2}hp((3a+2b)hm^2+6$a$hmhp+4$a$hp^2)s11^{2}sm+$b$hmhp^2(4$b$hm^2+6$b$hmhp+(2a+3b)hp^2)s11sm^2+b^2hp^{5}sm^3)(1+v)((a−b)(a+b)(2a^2+b^2(3+v))−2a^2b^2(3+v)(Log[a]−Log[b]))4B1^2($a$hms11+$b$hpsm)^2(−b^2(di−do)(1+v)+a^2(di+do+di$v$−do$v$))

Simplified Qgen:

Qgen=-((3 a b^2 B3 B4 B5 d31 di hm (hm+hp) p π s11 sm (1+v))/(4 B1^2 B6))

B4=(a^2 hm^5 $s11^3$+a hm^2 hp ((3 a+2 b) hm^2+6 a hm hp+4 a hp^2) $s11^2$ sm+b hm hp^2 (4 b hm^2+6 b hm hp+(2 a+3 b) hp^2) s11 sm^2+b^2 hp^5 sm^3) ;

(*B4==B1*)

B5=((a-b) (a+b) (2 a^2+b^2 (3+v))-2 a^2 b^2 (3+v) (Log[a]-Log[b]));

B6= (-b^2 (di-do) (1+v)+a^2 (di+do+di v-do v));

8. Derive the Expression of Capacitance

Cp=D[Qtotal,V3]

Cp= -1/($B1^2$ hp s11 (a hm s11+b hp sm)^2 (-1+v)) b^2 π (12 a^3 b B32 $d31^2$ hm^3 hp^2 (hm+hp)^2 $s11^3$ sm^2 (hm^3 s11+hp^3 sm)+6 a^4 $B3^2$ d312 hm^4 hp (hm+hp)^2 $s11^4$ sm (hm^3 s11+3 hm^2 hp sm+6 hm hp^2 sm+4 hp^3 sm)+a^2 hm^2 $s11^2$ (6 b^2 $B3^2$ $d31^2$ hp^3 (hm+hp)^2 sm^3 (4 hm^3 s11+6 hm^2 hp s11+3 hm hp^2 s11+hp^3 sm)+$B1^2$ (-2 $d31^2$-e33 s11 (-1+v)))+b^2 $B1^2$ hp^2 sm^2 (-2 $d31^2$-e33 s11 (-1+v))-2 a b $B1^2$ hm hp s11 sm (2 $d31^2$+e33 s11 (-1+v)))

Simplified Cp:

Cp=(b^2 π e33)/hp (1-(2 $K31^2$ B7)/(B4 (1-v)))

B7=B4-3 a^2 hm^2 hp (hm+hp)^2 $s11^2$ sm

9. Derive the Expression of Voltage output Vgen as function of Pressure P

Vgen=Qgen/Cp

Vgen= -((3 aB3 B4 B5 d31 di hm hp (hm + hp) s11 sm (1 + v))/(4 B1^2 B6 e33 (1 - (2 B7 K31^2)/(B4 (1 - v)))))P

APPENDIX B

SIMULATION CODE OF PRESSURE SENSORS

1. Fluid Pulse pressure sensor

```
hm=0.00017;
hp=0.00007;
% hp=0:0.00001:0.00080;
v=0.334;
vC=v;
vm=v;
vp=v;
e33=1527.*8.854.*10.^-12;

a=0.027/2;
b=0.015/2;

d31=-192.*10.^-12;
s11=2.271.*10.^-11;
ep=1/s11;
sm=1/(210.*10.^9);
em = 1/sm;

K31=-d31/sqrt(e33*s11);

c1=hp./(hp+hm);
c2=hm./(hp+hm);

% ec = c1.*ep + c2.*em + (c1.*c2.*ep.*em.*(vp - vm).^2)/(c1.*ep.*(1 - vm.^2)
+ c2.*em.*(1 - vp.^2));

ec=104*10^9; %equivalent stiffness of polyimide-PZT sandwiched part


di = (ec.*hp.^3)/(12.*(1 - vC));
do = (em.*hm.^3)/(12.*(1 - vm));
```

```
B1=2 .*a.* b.* hm.* hp.* s11.* sm.* (hm.^3.* s11 + hp.^3.* sm) + b.^2.*
hp.^2.* sm.^2.* (4 .*hm.^3.* s11 + 6.* hm.^2.* hp.* s11 + 3.* hm.* hp.^2.*
s11 + hp.^3.* sm) + a.^2 .*hm.^2.* s11.^2.* (hm.^3.* s11 + 3.* hm.^2.* hp.*
sm + 6.* hm.* hp.^2.* sm + 4 .*hp.^3.*sm);

B3=a.* hm .*s11 + b .*hp .*sm;

B4 = (a.^2.* hm.^5.* s11.^3 +    a.* hm.^2.* hp.* ((3.* a + 2 .*b).* hm.^2 +
6 .*a .*hm.* hp + 4 .*a.* hp.^2) .*s11.^2 .*sm +    b .*hm.* hp.^2.* (4 .*b.*
hm.^2 + 6.* b .*hm .*hp + (2 .*a + 3.* b) .*hp.^2) .*s11 .*sm.^2 +
b.^2 .*hp.^5.* sm.^3) ;

B5 = ((a - b) .*(a + b).*(2.* a.^2 + b.^2 .*(3 + v)) -2.* a.^2 .*b.^2 .*(3 +
v).* (log(a) - log(b)));

B6 = (-b.^2 .*(di - do) .*(1 + v) + a.^2 .*(di + do + di .*v - do.* v));

B7 = B4 - 3 .*a.^2.* hm.^2 .*hp.*(hm + hp).^2.* s11.^2.* sm;
Qgen=-3.* a.*b.^2 .*B3.* d31.* di.* hm.* (hm + hp) .*pi.* s11 .*sm.* (1 +
v).* B5./(4.* B1.*B6);

Cp = (b.^2 .*pi.* e33)./hp.* (1 - (2 .*K31.^2 .*B7)./(B1.* (1 - v)));

VgenTest=Qgen./Cp;
```

2. Air Blast Pressure Sensor

```
%Sample 1 and Sample 2

hm=0.00009;
hp=0.00012;
% hp=0:0.00001:0.00080;
v=0.344;
vC=v;
vm=v;
vp=v;
e33=2526.*8.854.*10.^-12;

a=0.015/2;
b=0.011/2;

d31=-190.*10.^-12;
s11=1.65.*10.^-11;

K31=-d31/sqrt(e33*s11);
ep=1/s11;
sm=1/(130.*10.^9);    %Brass Substrate
em = 1/sm;

c1=hp./(hp+hm);
c2=hm./(hp+hm);
```

```
ec = c1.*ep + c2.*em + (c1.*c2.*ep.*em.*(vp - vm).^2)/(c1.*ep.*(1 - vm.^2) +
c2.*em.*(1 - vp.^2));
% ec=104*10^9;


di = (ec.*hp.^3)/(12.*(1 - vC));
do = (em.*hm.^3)/(12.*(1 - vm));

B1=2 .*a.* b.* hm.* hp.* s11.* sm.* (hm.^3.* s11 + hp.^3.* sm) + b.^2.*
hp.^2.* sm.^2.* (4 .*hm.^3.* s11 + 6.* hm.^2.* hp.* s11 + 3.* hm.* hp.^2.*
s11 + hp.^3.* sm) + a.^2 .*hm.^2.* s11.^2.* (hm.^3.* s11 + 3.* hm.^2.* hp.*
sm + 6.* hm.* hp.^2.* sm + 4 .*hp.^3.*sm);

B3=a.* hm .*s11 + b .*hp .*sm;

B4 = (a.^2.* hm.^5.* s11.^3 +    a.* hm.^2.* hp.* ((3.* a + 2 .*b).* hm.^2 +
6 .*a .*hm.* hp + 4 .*a.* hp.^2) .*s11.^2 .*sm +    b .*hm.* hp.^2.* (4 .*b.*
hm.^2 + 6.* b .*hm .*hp + (2 .*a + 3.* b) .*hp.^2) .*s11 .*sm.^2 +
b.^2 .*hp.^5.* sm.^3) ;

B5 = ((a - b) .*(a + b).*(2.* a.^2 + b.^2 .*(3 + v)) -2.* a.^2 .*b.^2 .*(3 +
v).* (log(a) - log(b)));

B6 = (-b.^2 .*(di - do) .*(1 + v) + a.^2 .*(di + do + di .*v - do.* v));

B7 = B4 - 3 .*a.^2.* hm.^2 .*hp.*(hm + hp).^2.* s11.^2.* sm;

Qgen=-3.* a.*b.^2 .*B3.* d31.* di.* hm.* (hm + hp) .*pi.* s11 .*sm.* (1 +
v).* B5./(4.* B1.*B6);

Cp = (b.^2 .*pi.* e33)./hp.* (1 - (2 .*K31.^2 .*B7)./(B1.* (1 - v)));

VgenTest=Qgen./Cp;


%Sample 3
hm=0.00005;
hp=0.00007;
% hp=0:0.00001:0.00080;
v=0.3;
vC=v;
vm=v;
vp=v;

e33=1616.*8.854.*10.^-12;

a=0.0095/2;
b=0.009/2;
d31=-140.*10.^-12;
s11=1.65.*10.^-11;
ep=1/s11;
sm=1/(180.*10.^9);        % Iron Nickel Alloy Substrate

em = 1/sm;
```

```
K31=-d31/sqrt(e33*s11);
c1=hp./(hp+hm);
c2=hm./(hp+hm);

ec = c1.*ep + c2.*em + (c1.*c2.*ep.*em.*(vp - vm).^2)/(c1.*ep.*(1 - vm.^2) +
c2.*em.*(1 - vp.^2));
% ec=104*10^9;


di = (ec.*hp.^3)/(12.*(1 - vC));
do = (em.*hm.^3)/(12.*(1 - vm));

B1=2 .*a.* b.* hm.* hp.* s11.* sm.* (hm.^3.* s11 + hp.^3.* sm) + b.^2.*
hp.^2.* sm.^2.* (4 .*hm.^3.* s11 + 6.* hm.^2.* hp.* s11 + 3.* hm.* hp.^2.*
s11 + hp.^3.* sm) + a.^2 .*hm.^2.* s11.^2.* (hm.^3.* s11 + 3.* hm.^2.* hp.*
sm + 6.* hm.* hp.^2.* sm + 4 .*hp.^3.*sm);

B3=a.* hm .*s11 + b .*hp .*sm;

B4 = (a.^2.* hm.^5.* s11.^3 +    a.* hm.^2.* hp.* ((3.* a + 2 .*b).* hm.^2 +
6 .*a .*hm.* hp + 4 .*a.* hp.^2) .*s11.^2 .*sm +    b .*hm.* hp.^2.* (4 .*b.*
hm.^2 + 6.* b .*hm .*hp + (2 .*a + 3.* b) .*hp.^2) .*s11 .*sm.^2 +
b.^2 .*hp.^5.* sm.^3) ;

B5 = ((a - b) .*(a + b).*(2.* a.^2 + b.^2 .*(3 + v)) -2.* a.^2 .*b.^2 .*(3 +
v).* (log(a) - log(b)));

B6 = (-b.^2 .*(di - do) .*(1 + v) + a.^2 .*(di + do + di .*v - do.* v));

B7 = B4 - 3 .*a.^2.* hm.^2 .*hp.*(hm + hp).^2.* s11.^2.* sm;
Qgen=-3.* a.*b.^2 .*B3.* d31.* di.* hm.* (hm + hp) .*pi.* s11 .*sm.* (1 +
v).* B5./(4.* B1.*B6);

Cp = (b.^2 .*pi.* e33)./hp.* (1 - (2 .*K31.^2 .*B7)./(B1.* (1 - v)));

VgenTest=Qgen./Cp;
```

BIBLIOGRAPHY

1. Bu, Nan, et al. "A Flexible Piezoelectric Film Sensor for Fault Diagnosis of Pipe Systems." *Industrial Electronics Society, 2007. IECON 2007. 33rd Annual Conference of the IEEE*. IEEE, 2007.

2. Engineer's Toolbox: How to use differential pressure sensors to measure the hydrostatic level of a liquid in a vented or sealed tank. http://www.designfax.net/

3. Ohshima, Ichiro, et al. "Surfaces, Interfaces, and Films-Piezoelectric Response to Pressure of Aluminum Nitride Thin Films Prepared on Nickel-Based Superalloy Diaphragms." *Japanese Journal of Applied Physics-Part 1 Regular Papers and Short Notes* 45.6 (2006): 5169-5173.

4. Keck, Marian. "A new approach of a piezoelectric vibration-based power generator to supply next generation tire sensor systems." Sensors, 2007 IEEE. IEEE, 2007.

5. McLaughlin, J., et al. "Piezoelectric sensor determination of arterial pulse wave velocity." Physiological measurement 24.3 (2003): 693.

6. http://en.wikipedia.org/wiki/Piezoelectricity

7. Lu Dong, 'Research on the MEMS-based Piezoelectric Energy-based Piezoelectric Energy-harvesting Micro-Device', *MS Thesis, Shanghai JiaoTong University*, January 2007

8. Sunghwan Kim, 'Low power energy harvesting with piezoelectric generators', *PhD Thesis, Dept. of Mechanical and Material Science, University of Pittsburgh*, December 2002

9. Ramsay, Michael J., and William W. Clark. "Piezoelectric energy harvesting for bio-MEMS applications." SPIE's 8th Annual International Symposium on Smart Structures and Materials. International Society for Optics and Photonics, 2001.

10. www.piezocryst.com

11. PCB piezotronics: http://www.pcb.com/TechSupport/tech_gen

12. www.kistler.com

13. Kuoni, Andreas, et al. "Polyimide membrane with ZnO piezoelectric thin film pressure transducers as a differential pressure liquid flow sensor." Journal of Micromechanics and Microengineering 13.4 (2003): S103.

14. Akiyama, Morito, et al. "Flexible piezoelectric pressure sensors using oriented aluminum nitride thin films prepared on polyethylene terephthalate films." Journal of applied physics 100.11 (2006): 114318-114318.

15. Sensors, Piezo Film. "Technical Manual." Measurement Specialties Inc., www. msiusa. com (2008).

16. Shirinov, A. V., and W. K. Schomburg. "Pressure sensor from a PVDF film." Sensors and Actuators A: Physical 142.1 (2008): 48-55.

17. Marsili, Roberto. "Measurement of the dynamic normal pressure between tire and ground using PVDF piezoelectric films." Instrumentation and Measurement, IEEE Transactions on 49.4 (2000): 736-740.

18. Akitegetse, C., C. Volat, and M. Farzaneh. "Measuring bending stress on an ice/aluminium composite beam interface using an embedded piezoelectric PVDF (polyvinylidene-fluoride) film sensor." Measurement Science and Technology 19.6 (2008): 065703.

19. de Bruyne, P. "Piezo-electric film as a sensor element in signature verification. “Electrets, 1988.(ISE 6) Proceedings., 6th International Symposium on (IEEE Cat. No. 88CH2593-2). IEEE, 1988.

20. Fu, Y. Q., et al. "Recent developments on ZnO films for acoustic wave based bio-sensing and microfluidic applications: a review." Sensors and Actuators B: Chemical 143.2 (2010): 606-619.

21. Qin, Lifeng, et al. "Fabrication and characterization of thick-film piezoelectric lead zirconate titanate ceramic resonators by tape-casting." Ultrasonics, Ferroelectrics and Frequency Control, IEEE Transactions on 59.12 (2012): 2803-2812.

22. Mo, Changki, Leon J. Radziemski, and William W. Clark. "Analysis of piezoelectric circular diaphragm energy harvesters for use in a pressure fluctuating system." Smart Materials and Structures 19.2 (2010): 025016.

23. Vinson JR (1974) Structural Mechanics: The Behavior of Plates and Shells. John Wiley & Sons New York.

24. R.M. Christensen, Mechanics of Composite Materials, Wiley, New York, 1979.

25. http://ocw.mit.edu/courses/materials-science-and-engineering/3-11-mechanics-of-materials-fall-1999/modules/props.pdf.

26. Mohammadi, S., and M. Abdalbeigi. "Analytical Optimization of Piezoelectric Circular Diaphragm Generator." Advances in Materials Science and Engineering 2013 (2013).

27. http://www.pitt.edu/~qiw4/Academic/ME2082/Syllabus.htm

28. http://en.wikipedia.org/wiki/Piezoelectric_sensor

29. Tseng, Hong-Jie, Wei-Cheng Tian, and Wen-Jong Wu. "Flexible PZT thin film tactile sensor for biomedical monitoring." Sensors 13.5 (2013): 5478-5492.

30. http://en.wikipedia.org/wiki/Peristaltic_pump

31. McLaughlin, J., et al. "Piezoelectric sensor determination of arterial pulse wave velocity." Physiological measurement 24.3 (2003): 693.

32. Tadinada, Akhila. Piezo film sensor for capture of arterial wave pulse - Implementation. OpenStax-CNX. 19 Dec. 2007 <http://cnx.org/content/m15664/1.1/>.

33. "dorsalis pedis pulse." Mosby's Medical Dictionary, 8th edition. 2009. Elsevier 3 Jul. 2014 http://medical-dictionary.thefreedictionary.com/dorsalis+pedis+pulse

34. Reneer, Dexter V., et al. "A multi-mode shock tube for investigation of blast-induced traumatic brain injury." Journal of neurotrauma 28.1 (2011): 95-104.